

Analysis of the Quiescent State of BL Lacertae at Very High Energies

author: Julia Lascar

supervisor: Kenneth Ragan

A thesis submitted to McGill University in partial
fulfillment of the requirements of the degree of

Master of Science

McGill University, Montreal

Department of Physics

August, 2021

©Julia Lascar, 2021

Abstract

This thesis presents the analysis of archival data of the blazar BL Lacertae in the quiescent state and in the flaring state to investigate whether the source can be detected in the Very High Energy range (> 100 GeV, VHE) when it is not flaring, and if so, what its spectral properties are in that quiescent state. The variability of the source is studied using a Bayesian Block method. First, it considers the source's VHE gamma-ray emission with the ground-based gamma-ray observatory VERITAS. Then, for a multi-wavelength perspective, it analyses archival data from the Swift X-ray Telescope (0.3-10 keV energies), and from the Fermi Gamma-Ray Space Telescope (100 MeV-300 GeV energies). For each of these instruments, the quiescent state and flaring states of BL Lac are studied and compared.

Abrégé

Ce mémoire présente une analyse du blazar BL Lacertae dans son état de repos et dans son état de flamboiement, afin de voir si la source peut être détectée dans les Très Hautes Énergies (> 100 GeV, THE) lorsqu'elle n'est pas en période de flamboiement, et si oui, quelles sont ses propriétés spectrales dans cet état de repos. La variabilité de la source est étudiée à l'aide d'une analyse de Blocs Bayésiens. D'abord, on considère l'émission de la source en rayons gamma THE avec l'observatoire terrestre de rayons gamma VERITAS. Ensuite, afin d'obtenir une perspective à différentes longueurs d'ondes, on analyse les archives des données du Télescope Rayon-X Swift (énergies 0.2-10 KeV), et du Télescope Spatial Rayon-Gamma Fermi (énergies 100 MeV-300 GeV). Pour chacun de ces instruments, l'état de repos et l'état de flamboiement sont étudiés et comparés.

Acknowledgements

I would like to thank my advisor, Ken Ragan, for always being supportive, helpful, and kind. Thank you for guiding me and helping me become a better scientist. Thank you to post-doctoral students Ste O'Brien and Sajan Kumar, for answering my many questions and teaching me so much. To the VERITAS collaboration, whose vibrant community inspired and helped me, and in particular to Olivier Hervet for providing his valuable expertise and time to help with this project. Thank you to Daryl Haggard, for being an inspiration and making me feel welcome at McGill and more confident in myself. To Juan Gallego and Vladimir Khailenko, for their precious help with IT. To Tommy Burté, for his important advice. To Valérie Desharnais, for her great support and friendship. To Jemily Rime, for being a dear friend and cheering me on from start to finish. And finally, I would like to thank my parents, for always being there for me.

Statement of Original Contributions

- The author gathered and cleaned for quality the archival 12-year VERITAS data-set of BL Lacertae shown in this work, then used the software package EventDisplay to analyse this data set.
- The algorithm to analyse temporal variations in lightcurves with a Bayesian Block method used Astropy's bayesian block function and the author's original code.
- Monte-Carlo simulations of gamma-ray showers using the CORSIKA package were produced, and used to train a set of boosted decision trees for gamma/hadron separation, as seen in Figures 3.5 to 3.10.
- Archival data set of BL Lacertae observed by *Fermi*-LAT was gathered and analysed by the author.
- Archival data set of BL Lacertae observed by Swift-XRT was gathered and analysed by the author.
- Finally, the author took on remote observing shifts for the VERITAS telescope as part of their duty to the collaboration.

Table of Contents

Abstract	1
Abrégé	2
Acknowledgements	3
Statement of Original Contributions	4
List of Figures	9
List of Tables	10
1 Introduction	11
1.1 Very High Energy Astrophysics	12
1.1.1 Hadronic Processes	12
1.1.2 Leptonic Processes	13
1.1.3 VHE Sources	15
1.2 Active Galactic Nuclei	15
1.2.1 Unified AGN Scheme	16
1.2.2 Blazars	18
1.2.3 Models of VHE gamma-ray production	19
2 The VERITAS Telescope Array	23
2.1 The Imaging Atmospheric Cherenkov Technique	24
2.1.1 Electromagnetic Air Showers	25
2.1.2 Hadronic Air Showers	27
2.2 VERITAS Instrumentation	30

2.2.1	General Design	30
2.2.2	Trigger System	33
3	BL Lacertae Analysis	35
3.1	Analysis Tools	35
3.1.1	VERITAS Standard Analysis	35
3.1.2	Boosted Decision Trees for Gamma/Hadron separation	41
3.1.3	Bayesian Block Analysis	51
3.2	Analysis Results	53
3.2.1	Full archival data set and quality cuts	53
3.2.2	Identifying Flares	56
3.2.3	BL Lac in the quiescent state	58
4	BL Lacertae as seen by Fermi-LAT and Swift-XRT	62
4.1	<i>Fermi</i> -LAT	62
4.1.1	Data Selection	64
4.1.2	Quiescent State Analysis	66
4.2	Swift-XRT	70
4.2.1	Data Selection	71
4.2.2	Quiescent State Analysis	73
5	Conclusions	78

List of Figures

1.1	A schematic diagram of bremsstrahlung radiation.	14
1.2	A schematic diagram of synchrotron radiation.	15
1.3	Sky Map of the 243 VHE sources in the TeV range, as reported by TevCat (2021).	16
1.4	Diagram of blazar classification based on viewing angle.	17
1.5	A simplified diagram of the spectral energy distribution of BL Lac objects. .	20
2.1	Schematic views of Cherenkov emission.	25
2.2	Schematic view of an electromagnetic cascade in the atmosphere induced by a VHE gamma-ray.	26
2.3	A survey of the all-particle cosmic ray spectrum.	28
2.4	Schematic view of a hadronic air shower.	29
2.5	Monte Carlo simulations of gamma-ray and cosmic-ray air showers gener- ated with the CORSIKA package.	30
2.6	Photo of the VERITAS array, located at the Fred Lawrence Whipple Obser- vatory, in Arizona, United States.	31
2.7	Overhead view of VERITAS.	31
2.8	Photograph of the VERITAS camera with and without Winston cones. . . .	32
3.1	Two typical FADC traces.	36
3.2	Pixel (PMT) information before and after cleaning.	37
3.3	Hillas parameterization of shower images.	38

3.4	Examples of geometrical reconstruction.	39
3.5	Distribution of mean-scaled width vs mean-scaled length for a background training sample	43
3.6	Distribution of mean-scaled width vs mean-scaled length for a signal training sample	43
3.7	Distribution of shower emission height for a background training sample (data) vs signal (simulation).	44
3.8	Distribution of the χ^2 of shower emission height for a background training sample vs signal.	45
3.9	Distribution of the second largest image's size for a background training sample vs signal.	45
3.10	Distribution of the distance to shower core for a background training sample vs signal.	46
3.11	Examples of how energy and zenith angle affect the distribution of discriminating variables.	46
3.12	Visual representation of a decision tree's development.	47
3.13	Efficiency of background and signal as a function of cut value, and signal significance as a function of cut value.	50
3.14	Two contrasting examples of L3 rate that do and do not require time cuts.	54
3.15	The lightcurve of BL Lac over 11 years of data, binned nightly.	55
3.16	Smoothed significance skymap of the full data set of BL Lac.	56
3.17	Light curve of BL Lac with Bayesian Block bins.	57
3.18	Smoothed significance skymap of BL Lac in the quiescent state.	59
3.19	Comparison of the BL Lac energy spectrum in the flaring state and in the quiescent state.	61
4.1	Artist's rendition of the Fermi Gamma-Ray Space Telescope.	63
4.2	The <i>Fermi</i> -LAT five-year all-sky map.	63
4.3	All sky map of <i>Fermi</i> -LAT sources as reported in their eight-year catalogue.	64

4.4	<i>Fermi</i> -LAT Lightcurve of BL Lac	65
4.5	<i>Fermi</i> -LAT Lightcurve of BL Lac with Bayesian Block bins.	65
4.6	Counts map of BL Lac in the quiescent state as seen by <i>Fermi</i> -LAT.	67
4.7	Best fit spectra of BL Lac and background sources.	68
4.8	Best fit spectrum of BL Lac in the quiescent state as seen by <i>Fermi</i> -LAT.	68
4.9	Best fit spectrum of BL Lac in the flaring state as seen by <i>Fermi</i> -LAT.	69
4.10	Plot of the best-fit model of BL Lac as seen by <i>Fermi</i> -LAT.	70
4.11	Artist's rendition of the Neil Gehrels Swift Observatory	71
4.12	Swift-XRT light-curve of BL Lacertae.	72
4.13	Swift-XRT light-curve of BL Lacertae with Bayesian Block bins.	72
4.14	Sky map of BL Lac in the quiescent state as seen by Swift-XRT.	74
4.15	Quiescent spectra of BL Lac as seen by Swift-XRT.	75
4.16	Flaring spectra of BL Lac as seen by Swift-XRT.	76
4.17	Plot of the best-fit model of BL Lac as seen by Swift-XRT.	77

List of Tables

3.1	Properties of the total BL Lac data set.	55
3.2	Flares as determined by the Bayesian Block analysis.	58

Chapter 1

Introduction

Blazars, a type of Active Galactic Nuclei (AGN), are some of the brightest and most variable sources of Very High Energy (>100 GeV) gamma-rays in the sky. They are most often observed when "flaring", a state in which their flux can be orders of magnitude higher than average. In order to study these sources adequately, however, one needs to also look at the "quiescent" state, when the source is not flaring. This thesis considers the blazar BL Lacertae in its quiescent state, and asks whether it significantly emits in the VHE range when it is quiescent, and what are its spectral properties in the quiescent state compared to the flaring state. We then look to other energies: X-ray, and lower energy gamma-rays. We find that for the three studied wavelengths bands, BL Lacertae is detectable in the quiescent state and displays different spectral properties from when it is flaring.

This introduction covers important astrophysical context. It starts with a review of VHE astrophysics, describing relevant particle physics processes and types of astrophysical VHE sources, then, it introduces the unified AGN scheme, and in particular, blazars. A short overview of common blazar VHE emission models is given.

1.1 Very High Energy Astrophysics

Gamma-rays are photons on the most energetic part of the electro-magnetic spectrum, with energies above a few MeV. In particular, the Very High Energy (hereafter VHE) domain corresponds to the energies above 100 GeV. This radiation is of great importance for astrophysics; it is produced in exotic, high-energy environments, notably ones that might also generate cosmic rays (charged astroparticles such as hadrons and leptons that have yet to be associated to a single source [Kotera and Olinto, 2011]). Unlike cosmic rays, however, photons are not charged, and thus VHE gamma rays are not deflected by magnetic fields. This means that VHE photons are excellent messenger particles that can be retraced to sources far out of our galaxy.

An important aspect of VHE gamma-rays is that, unlike most astrophysical electro-magnetic radiation, they are not generated through black-body radiation. Above a few keV, radiation can only be generated by non-thermal processes. Sections 1.1.1 and 1.1.2 describe some of the processes relevant to VHE astronomy and BL Lac, separating them in two: leptonic processes, and hadronic processes.

1.1.1 Hadronic Processes

Hadronic processes mainly involve interactions between protons and nuclei, which generate neutral and charged pions [Aharonian et al., 2013]. This process of pion production is most effective in high-density environments, because a higher density of nuclei targets leads to a higher interaction rate. The neutral pion (π^0) has a short lifetime of about 10^{-16} s, and will usually decay into two gamma rays (eq 1.1) — although one percent of the time it will instead lead to a gamma-ray and an electron-positron pair (eq 1.2). Neutral pion decay is at the heart of hadronic models of gamma-ray emission.

$$\pi^0 \rightarrow \gamma + \gamma \tag{1.1}$$

$$\pi^0 \rightarrow \gamma + \gamma + e^+ + e^- \quad (1.2)$$

Charged pions have a longer lifetime (about 10^{-8} s), and they will generate neutrinos and muons when they decay.

$$\pi^\pm \rightarrow \mu^\pm + \nu_\mu \rightarrow e^\pm + \nu_e + \bar{\nu}_\mu + \nu_\mu \quad (1.3)$$

1.1.2 Leptonic Processes

Leptonic processes, on the other hand, refer to the interactions between relativistic electrons and positrons with either low-energy photon fields (inverse Compton scattering), or electromagnetic fields (bremsstrahlung and synchrotron radiation). The latter produce lower-energy gamma rays, whereas Inverse Compton Scattering can excite photons up to VHE energies [Aharonian et al., 2013].

Inverse Compton Scattering Inverse Compton scattering refers to the relativistic version of Thomson scattering. Low-energy photons scatter off of relativistic electrons, resulting in a higher energy photon. In the classical case of Thomson scattering, the cross-section of this process is:

$$\sigma_T = \frac{8}{3}\pi r_e^2 \quad (1.4)$$

but at relativistic energies, we need to use the ultra-relativistic version of the Klein-Nishina formula (which gives the differential cross section of photons scattered from a single free electron in quantum electrodynamics). Electrons undergo large energy losses, and following Wagner [2006], it can be shown that the photons can achieve a maximum energy of:

$$E_{max} \approx 4\gamma^2 E_\gamma \quad (1.5)$$

Where E_γ is the energy of the incoming photon and γ is the Lorentz factor. So, in cases where the Lorentz factor of the electron is in the $10^2 - 10^3$ range, keV photons (such as

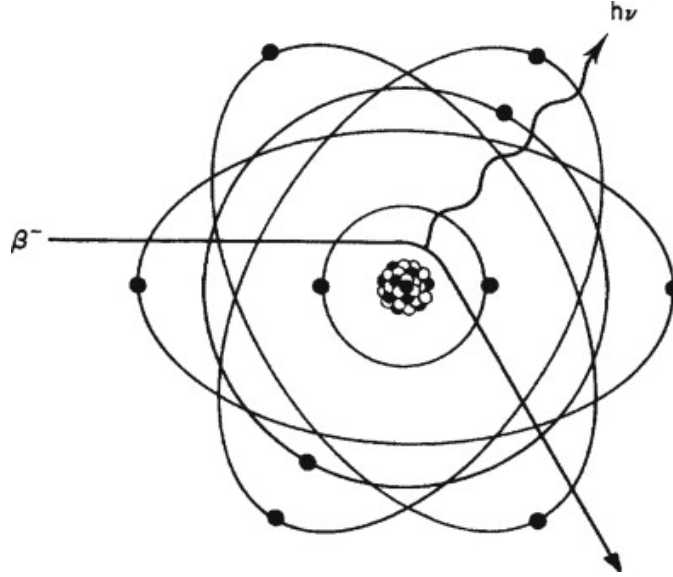


Figure 1.1: A schematic diagram of bremsstrahlung radiation, from L'Annunziata [2003].

those from Synchrotron radiation, as explained below) can be upscattered to the VHE range.

Bremsstrahlung Bremsstrahlung (from the German 'braking radiation'), is the radiation emitted by charged particles when they pass through an electric field and change speed or direction (See Figure 1.1). This process is essential to air-shower physics (see section 2.1 [Stecker, 1971]).

Synchrotron radiation Synchrotron radiation is emitted when highly relativistic electrons are accelerated by a magnetic field (See Figure 1.2). The peak energy emitted is:

$$E_{peak} = 5 \times 10^{-9} B_{\perp,G} \gamma_e^2 \text{ eV} \tag{1.6}$$

where γ_e is the electron Lorentz factor, and B_{\perp} , is the transverse component of the magnetic field in Gauss. This process is essential to leptonic models of VHE emission in Active Galactic Nuclei (see section 1.2.3), as photons generated through synchrotron radiation will be typically in the keV range, and can be upscattered to VHE energies via the Inverse Compton process.

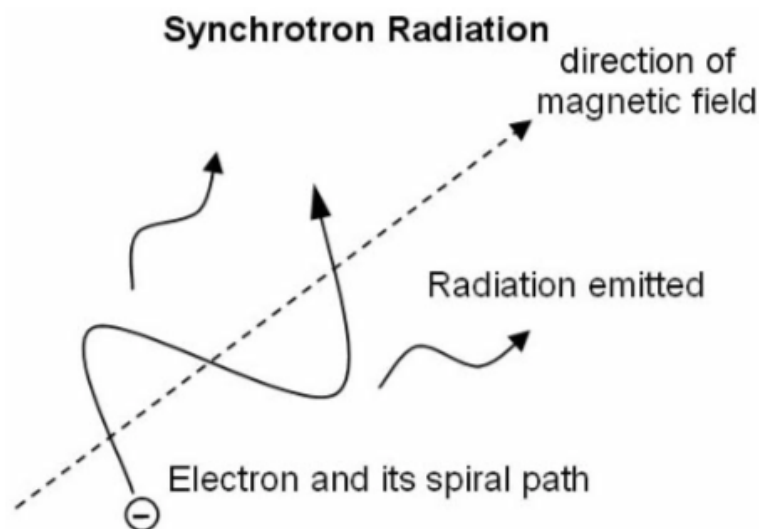


Figure 1.2: A schematic diagram of synchrotron radiation. From Stanger [2004].

1.1.3 VHE Sources

After decades of gamma-ray astronomy, hundreds of astronomical VHE sources have been discovered. As of June 2021, TeVCat [Wakely and Horan, 2008] reports 243 sources detected in the TeV range (see Figure 1.3). At the galactic scale, sources include supernova remnants, pulsars, microquasars, and more. At the extragalactic scale, sources have been detected up to a redshift of ≈ 1 , and consist mostly of a type of Active Galactic Nuclei (AGN) called blazars. The following section will explore this type of source in more detail.

1.2 Active Galactic Nuclei

In this section, I explain types of active galactic nuclei and the prevailing paradigm that explains their structure.

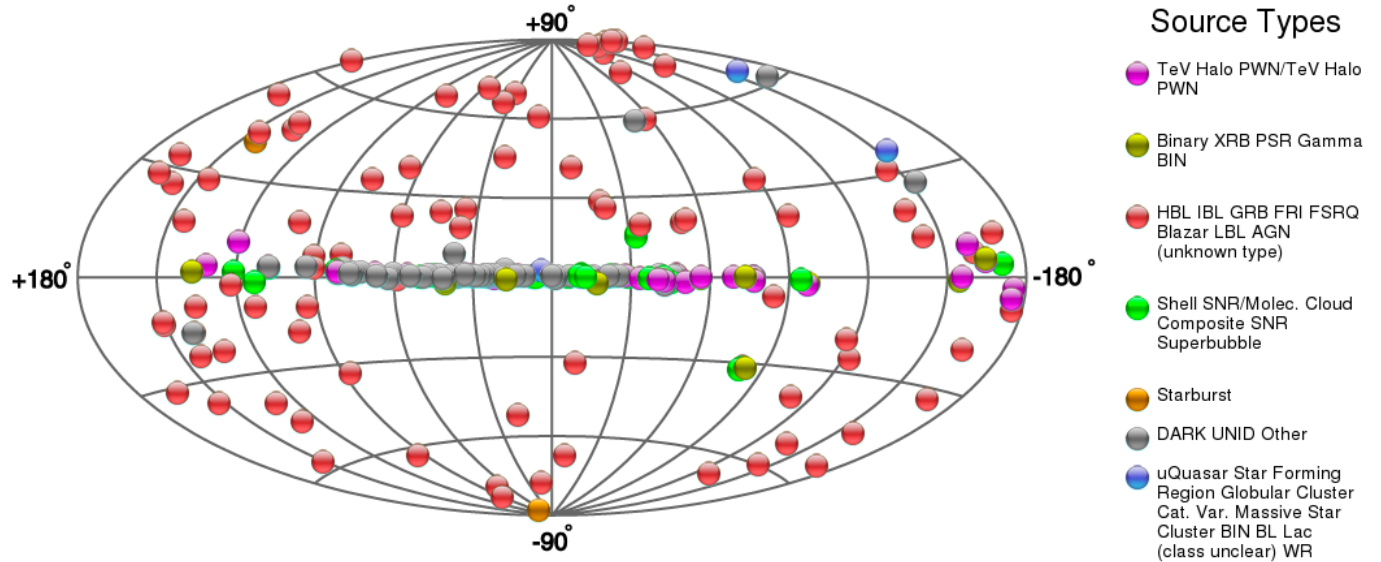


Figure 1.3: Sky Map of the 243 VHE sources in the TeV range, as reported by TevCat (2021).

1.2.1 Unified AGN Scheme

About one percent of galaxies display special central regions with high energy processes that cannot be thermal or nuclear in origin (such as those at play in stars). Called Active Galactic Nuclei (hereafter AGN), these regions are very luminous and dense: 10^6 to 10^{10} solar masses (M_{\odot}) contained in the size of our solar system [Robson, 1996].

AGNs come in subclasses with very different properties, but these classes are brought together in the theory of the unified AGN scheme, which sees them as similar objects viewed from different angles (see Figure 1.4). They are further separated based on whether or not they are radio-loud, on their evolutionary state, and accretion rate (see for example Alexander and Hickox [2012]).

According to this scheme, AGNs have a central supermassive blackhole (SMBH) that accretes the matter that surrounds it, forming a hot plasma disk (called the accretion disk). In the turbulence of the accretion disk, gravitational energy is transformed into thermal radiation, which then excites and ionizes the fast-moving gas cloud near the SMBH. In

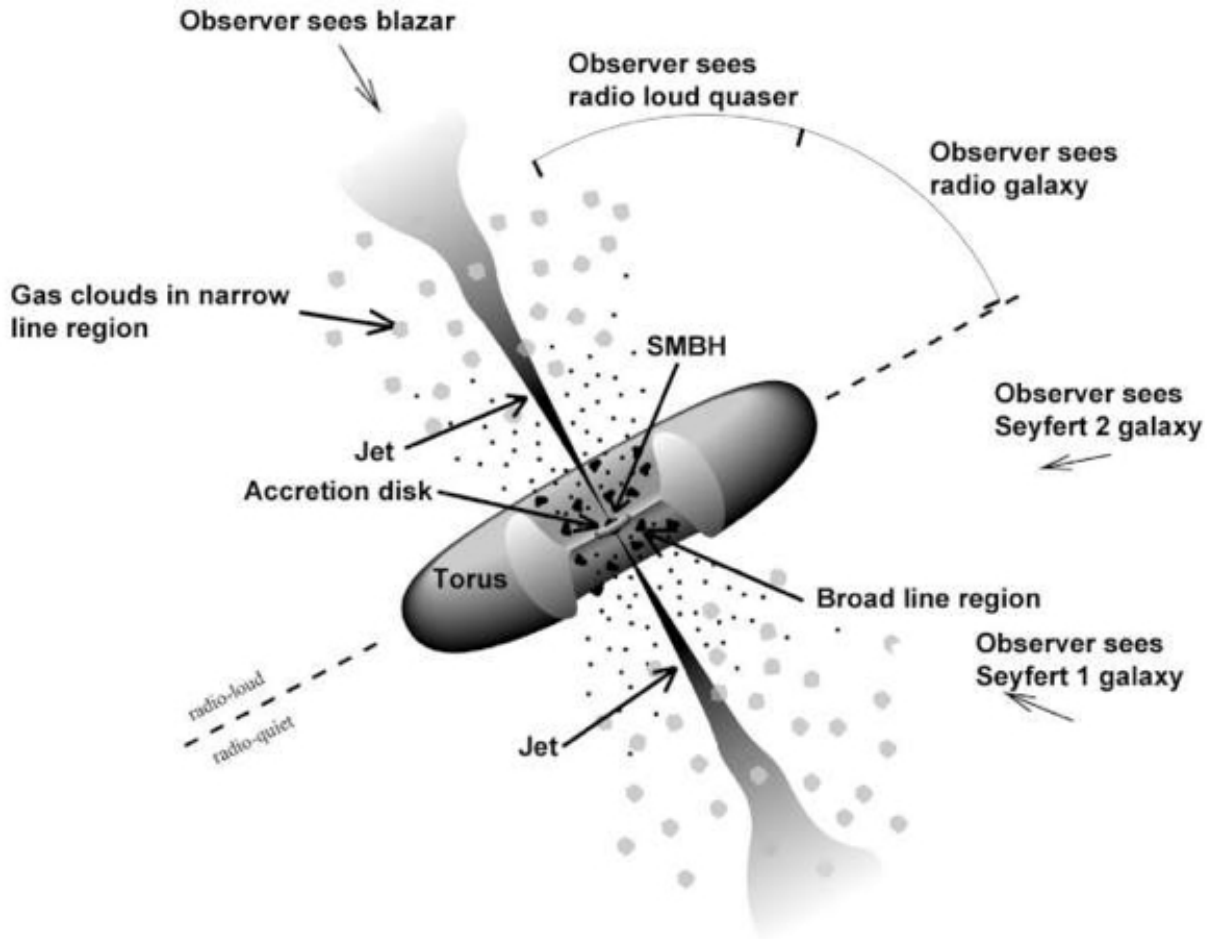


Figure 1.4: From Myers [2016], a diagram of the unified AGN scheme that focuses on how the observer’s viewing angle and the loudness of the radio emission changes the type of AGN. Viewed head-on and radio-loud, we call the AGN a blazar (see section 1.2.2).

that part of the AGN, the spectrum thus displays Doppler-broadened emission lines, which is why the centre is dubbed the ‘broad-line region’.

Further from the center, molecular clouds are slower by a factor of 10, and their emission lines are in turn less Doppler-broadened: this is the ‘narrow-line region’. Around the system, a dust torus conceals the center of the AGN along the equatorial plane. Another remarkable feature in some AGNs are jets: two ultra-relativistic plasma beams perpendicular to the accretion disk. These jets are caused by a strong magnetic field, which supports

the theory of a fast-rotating body at the center, such as a SMBH. It would in effect act as a gyroscope, capable of sustaining stable jets for a long period of time.

1.2.2 Blazars

Blazars, short for 'blazing quasars', are an especially interesting type of AGN for VHE astronomy. Most extragalactic emitters of VHE gamma-rays are blazars [Wakely and Horan, 2008]. They are defined by a jet structure in close alignment with the observer's line of sight (the jet beams towards us). In other AGNs, when they are seen from the side, we observe twin jets that extend into intergalactic space at huge scales: from kiloparsecs up to megaparsecs. In blazars, where the jet axis is towards our line of sight, the approaching jet is Doppler-brightened, whereas the receding one is dim and harder to observe. [Wagner, 2006]

Turbulence in the jet accelerates particles, emitting non-thermal radiation over an energy range that spans from radio to VHE — 20 orders of magnitude. Radiation from the jet is bright enough to almost completely mask the host galaxy's surrounding thermal emission.

Blazars can further be subdivided into subclasses: flat spectrum radio quasars (FSRQ), defined by strong and broad emission lines, and "BL Lac" objects, based on the source that is the subject of this thesis, which barely show any emission lines [Landt et al., 2004].

In both cases, one of the main characteristics of blazars is their variability on multiple wavelengths and timescales. Their electromagnetic emission levels can change by more than one order of magnitude, dubbed "flares". Some blazars, such as Mkn 501 [Xue and Cui, 2005], were found to have a low steady-state emission (or quiescent state) with intermittent flares that could go as high as 10 times the flux of the brightest source of gamma-rays in the sky, the Crab Nebula, a young supernova remnant.

In this thesis, I investigate whether BL Lacertae emits in the VHE regime when it is quiescent, and if so, what spectral properties does that emission display.

1.2.3 Models of VHE gamma-ray production

The Spectral Energy Distributions (SED) of BL Lac blazars display two broad peaks: the lower energy one can be found anywhere between radio and x-ray, while the high energy one is typically in the MeV regime or higher. Depending on the energy range of these peaks, BL Lac blazars can be separated in three types: low energy-peaked BL (LBL), intermediate energy-peaked BL (IBL), and high energy-peaked BL (HBL), (see Figure 1.5). At VHE energies, the spectra of BL Lacs often take the shape of a power-law with a spectral index Γ . The spectral index is an important parameter for theoretical modelling of VHE emissions.

The lower energy peak of the SED is commonly attributed to synchrotron radiation, but the origin of the high energy bump is more controversial. Two competing models emerge in the literature: those based on leptonic emission, and those based on hadronic emission.

Leptonic Models The defining feature of leptonic models is that they explain the high-energy bump of the SED as originating from inverse Compton scattering of lower energy photons by relativistic electrons. In some models, the source photon field is itself produced by synchrotron radiation from the same relativistic electrons that then trigger inverse Compton. The phenomenon is then called synchrotron self-compton (SSC) [Ghisellini, 2013]. In other models, the source photon field might be external, such as coming from the accretion disk, the broad-line region, the torus, or from slower/faster moving regions of the jets [Boettcher, 2019].

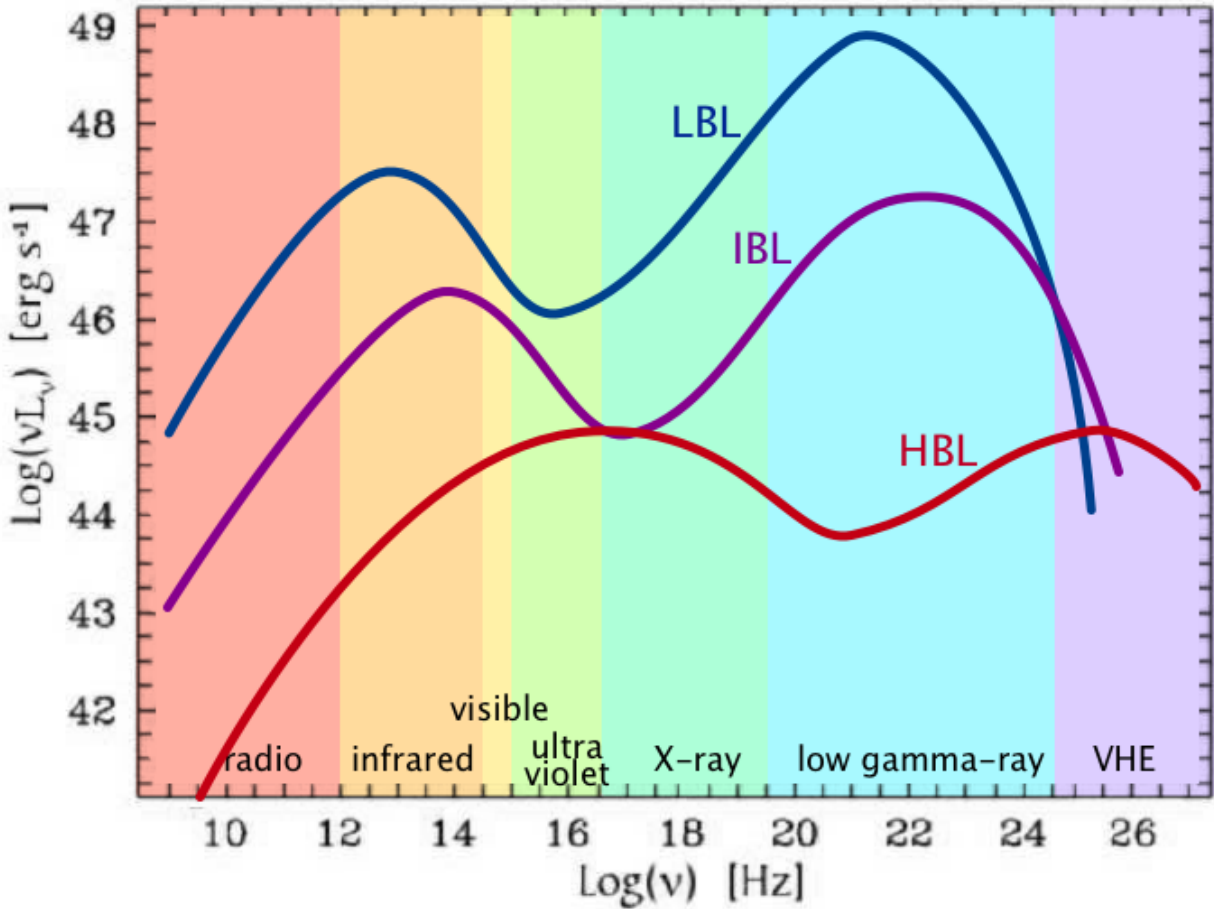


Figure 1.5: A simplified diagram of the spectral energy distribution of BL Lac objects. Three general types exist based on the location of the broad lower-energy peaks. In blue, the low BL (LBL). In purple, the intermediate BL (IBL). In red, the high BL (HBL). Inspired from data in Ciprini et al. [2003], where the SED of several BL blazars were averaged.

Leptonic models postulate that the radiation is dominated by electrons and/or electron-positron pairs, but most models usually also account for the presence of protons of classical or mildly-relativistic energies. These are however not considered to contribute significantly to the radiative output, though they may influence the mechanics and kinematics of the jet significantly (see, for instance, Sikora and Madejski [2000]).

Hadronic Models Hadronic models, on the other hand, usually assume that protons are being accelerated to ultra-relativistic energies, and thus explain the high-energy bump of

the SED with proton-synchrotron radiation (see Mücke and Protheroe [2001]), or with photon-pion production followed by pion decay that generates ultra-high-energy photons, electron-positron pairs, and neutrinos (see Mannheim and Biermann [1992]).

The latter is especially important when considering the development of multi-messenger astronomy. Detecting a VHE neutrino source coinciding with a VHE gamma-ray source can be a strong argument for hadronic models. For instance, the neutrino detector IceCube [Aartsen et al., 2017] registered a 290 TeV neutrino in September 2017 (event 170922A) and reconstructed its origin as coinciding with the blazar TXS 0506+056 (a BL-Lac object) [IceCube Collaboration et al., 2018]. VERITAS and MAGIC, two ground-based gamma-ray telescopes, followed up on the source and found no excess simultaneous gamma-ray emission, though the AGILE satellite did detect an excess. Further archival research of IceCube data found an excess of neutrino events from the direction of TXS 0506+056 between September 2014 and March 2015 with a confidence level corresponding to 3.5σ . While this is not a clear-cut case, comparing observations at different wavelengths and different messenger particles can bring key information to favor or discard emission models, and future generations of neutrino detectors and gamma-ray telescopes will undoubtedly help shed light on the matter.

Chapter 2 gives an overview of the VERITAS telescope array, the main instrument used for this thesis. After reviewing the general Imaging Atmospheric Cherenkov Technique used by most ground-based gamma-ray telescopes, we look more specifically at the VERITAS instrumentation and design.

Chapter 3 describes the analysis of BL Lac in the quiescent state as seen by VERITAS. First, the VERITAS standard analysis is described, followed by the technique of boosted decision trees for signal/background separation, and the Bayesian Block method used to study the variability of the BL Lac light-curve and which time intervals should be marked as quiescent. Then, the results of the VHE analysis is shown, and the quiescent state is compared to the flaring state.

Chapter 4 looks at BL Lac data at other energies: first in the lower energy gamma-rays (100MeV-300GeV) with *Fermi*-LAT, then in the X-rays (0.3-10keV) with Swift-XRT.

Finally, we make our concluding remarks in Chapter 6.

Chapter 2

The VERITAS Telescope Array

The greatest obstacle to VHE astronomy is that the Earth's atmosphere is opaque to gamma-rays. While this protects us from any possible nefarious impact these particles could have on our health, it makes it impossible to directly observe gamma-rays from the ground.

A possible solution is then to observe the particles from space, by putting a satellite-based telescope in orbit, as was done with *Fermi*-LAT, but this faces several problems. Firstly, astro-engineering endeavours are extremely expensive and high-risk. Secondly, VHE processes typically display a steeply falling power-law spectrum, meaning that the flux of VHE gamma rays is very low.

As an example, above 1 TeV, the Crab Nebula (a supernova remnant and the brightest source of gamma-rays in our sky) generates merely ~ 6 photons per m^2 per year at the Earth. A satellite-based telescope would need to be huge to detect such a low flux, which would be both expensive and impractical. It is in part due to this constraint that *Fermi*-LAT's upper energy limit is around 300 GeV.

One solution is provided by the ground-based Imaging Atmospheric Cherenkov Technique, first studied by Galbraith and Jelley [1953], and whose concept was proven with

the detection of the Crab Nebula by the Whipple 10m Telescope [Weekes et al., 1989]. By making use of the atmosphere as a part of the detector, Imaging Atmospheric Cherenkov Telescopes (IACTs) turn the opaque atmosphere into an asset, and can obtain an effective collecting area of over 10^4m^2 , detecting gamma-rays through a relatively wide field of view with good angular and energy resolutions, making them the most sensitive VHE gamma-rays detectors. In this section, I will review this technique, and how it has been implemented with VERITAS.

2.1 The Imaging Atmospheric Cherenkov Technique

When a VHE particle enters the Earth's atmosphere, its interaction with air molecules induces an extensive air shower, i.e., a cascade of charged and neutral particles. Since these secondary particles are relativistic and may travel faster than the speed of light in air, they will generate Cherenkov radiation, producing a conic pool of blue to ultra-violet light.

Cherenkov radiation is emitted whenever a charged particle travels through a dielectric medium at a speed greater than the speed of light in that medium. The charged particle polarizes the medium around it, exciting the medium's molecules which then emit photons as they return to their ground state. But the speed of these photons in the medium is lower than the speed of the primary particle, so we observe the formation of a waveform that looks like a conical "shock front" [Cogan, 2006] (See Figure 2.1).

A telescope located within that cone of light, and pointing towards the source of the shower, can thus capture the projection of the light cone on the ground. Such an event will be very short, lasting 4-8 ns. If an array of telescopes record the image from several point of views, a stereoscopic technique can be used to reconstruct the properties of the inducing (primary) particle. The way VERITAS accomplishes this is described in more detail in section 2.2.

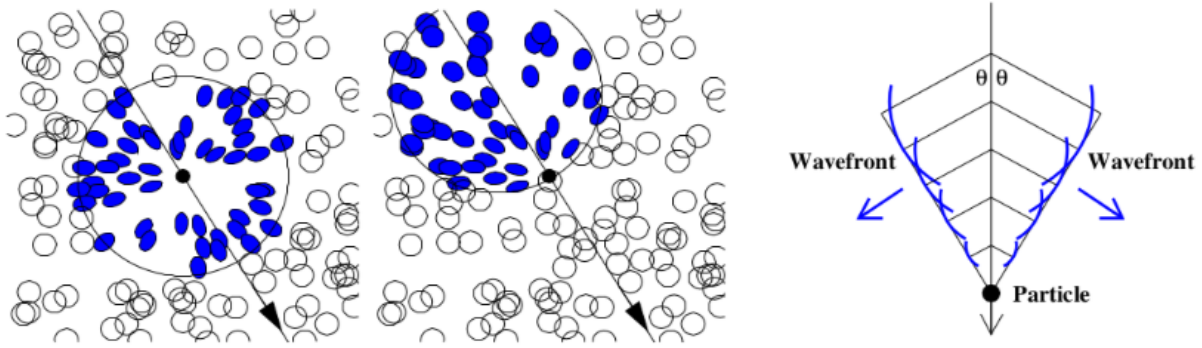


Figure 2.1: Left: Schematic view of Cherenkov emission resulting from coherent polarization in a medium. Right: Huygens construction of the Cherenkov emission angle. [Cogan, 2006].

The properties of the secondary shower are directly dependent on the primary particle's energy, nature, and direction. In particular, showers generated by gamma rays (called electromagnetic showers) do not have the same shape as those generated by hadrons (hadronic showers). This difference is especially important for gamma-ray astronomy, where (usually), VHE photons are the signal we want to detect, and hadrons are the background we want to suppress. In the following two sections, I explain the differences and similarities of the two types of showers; section 3.1.2 will explain how the VERITAS analysis uses machine learning to separate electromagnetic signals from hadronic background.

2.1.1 Electromagnetic Air Showers

A gamma-ray hitting a nucleus can produce an electron and positron pair if the photon has more energy than twice the electron's rest mass, i.e., $E_0 > 2 \times 0.511 \text{ MeV}$.

$$\gamma \rightarrow e^+e^-, \quad (2.1)$$

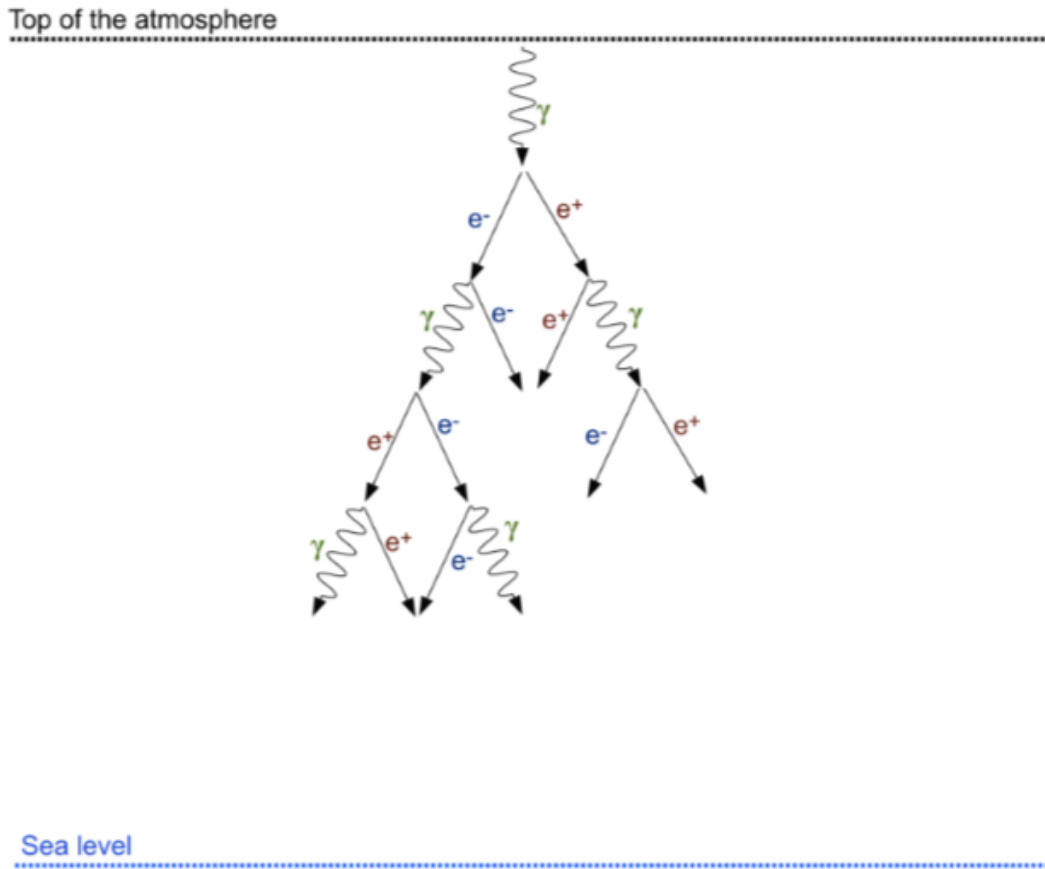


Figure 2.2: Schematic view of an electromagnetic cascade in the atmosphere induced by a VHE gamma-ray. Figure from Gammell [2004].

where the presence of the nucleus is necessary to conserve the energy and momentum of this reaction. The electron and positron share the energy of the primary photon. When the primary particle is a VHE gamma-ray, the two leptons will be highly relativistic and radiate new VHE photons through Bremsstrahlung, which will then themselves have a chance to undergo pair-production, starting the process again. This loop (which is shown schematically in Figure 2.2) will occur many times, generating a shower of relativistic electrons and positrons, and thus, Cherenkov radiation (from the electrons and positrons). The particle shower continues to develop with each "generation" of electrons becoming of lower energy, until they reach a critical energy $E_c \approx 84$ MeV. At this energy threshold,

Bremsstrahlung and ionization energy loss rates are approximately equal. This marks the maximum shower development, X_{max} , when ionization losses begin to take over. The number of particles in the cascade decreases quickly, ending the air-shower. Because the particles in electromagnetic showers also undergo multiple Coulomb scattering, their velocities are distributed over a small range of angles, and the shower's lateral extent is relatively narrow.

These showers are formed exclusively of electrons, positrons, and photons. Intuitively, the total number of these particles is proportional to the energy of the primary photon: the higher the primary energy, the longer the air shower will last, and the more particles will be generated, and the more Cherenkov light will be emitted. IACTs make use of this property when reconstructing the energy of the primary particle (see section 4.1.1).

Another type of electromagnetic air shower is one induced by electrons and positrons. These are almost indistinguishable from photon-initiated air showers, with only a slight difference in the depth of first interaction in the atmosphere, and are a part of the background that needs to be accounted for, but their flux is much less than that of the primary background, namely hadronic particles.

2.1.2 Hadronic Air Showers

The majority of VHE particles that hit the atmosphere are not gamma-rays, but instead hadrons, dubbed cosmic rays (CRs): protons (86%), helium nuclei, (11%), heavier nuclei (1%), and a small admixture of electrons and positrons (2%). They are charged and can reach highly relativistic energies [Longair, 2011]. Figure 2.3 shows the CR spectrum, which exhibits a power law structure up until a break called the "knee", around 10^{15} eV.

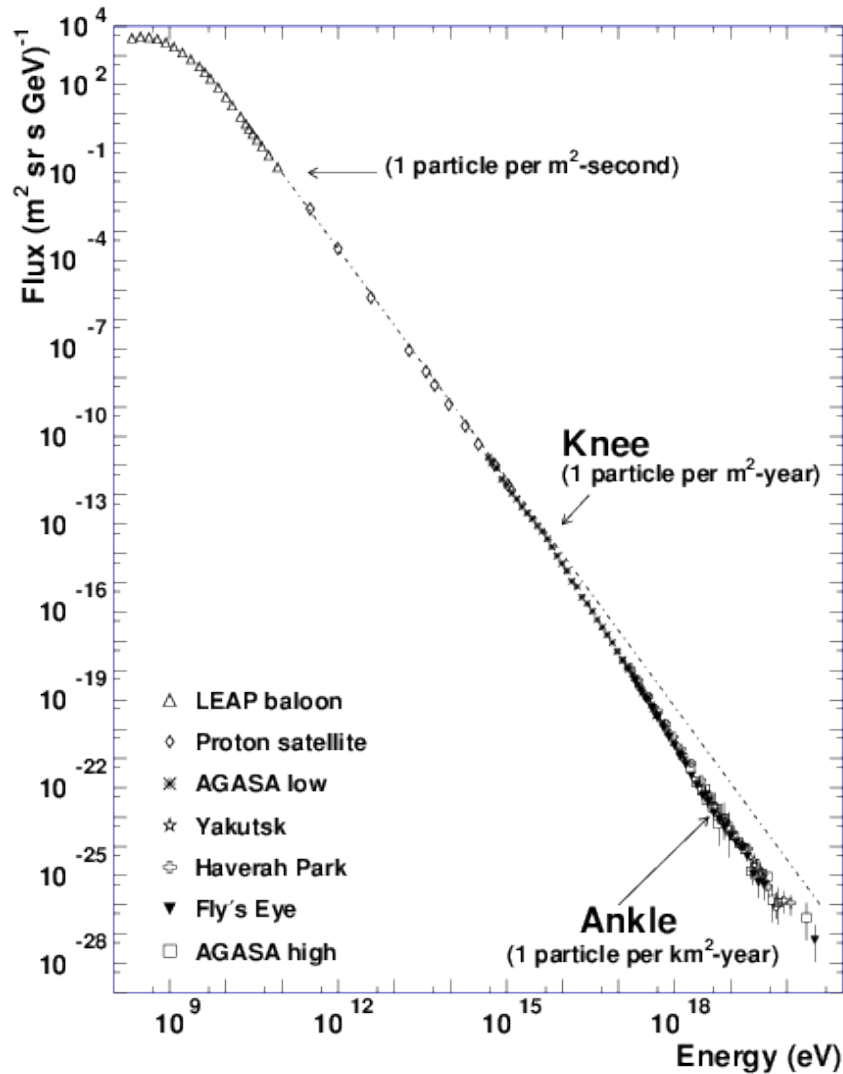


Figure 2.3: A survey of the all particle cosmic ray spectrum with data from seven different instruments. The spectrum follows a power law fit remarkably well up to the so-called “knee”. From Wilkens et al. [2003].

The development of hadronic showers is more complex than electromagnetic showers. Interactions with nuclei in the air induce the production of secondary nucleons, pions (charged and neutral), and muons, which quickly decay, as was introduced in section 1.1.1. Figure 2.4 shows a schematic diagram of the development of a hadronic air-shower, and the resulting hadronic, muonic, and electromagnetic components.

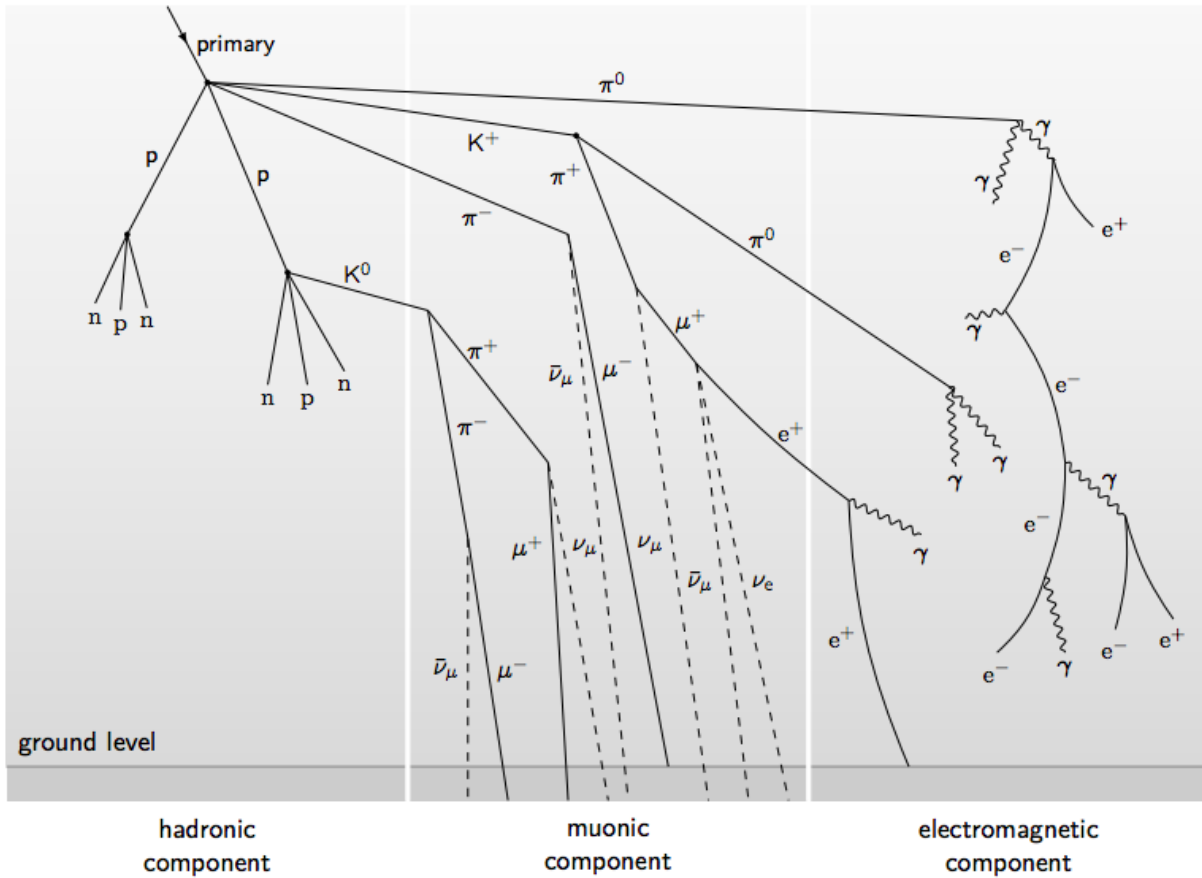


Figure 2.4: From Krause [2017], a schematic view of a hadronic air shower.

Muons from charged pions will have long lives and reach the ground, only losing energy via Cherenkov radiation and ionization. On the other hand, neutral pions will generate VHE gamma-rays, triggering a secondary electromagnetic sub-shower. Because pions from CR-induced showers usually have large transverse momenta, hadronic air showers generally display a larger lateral spread than their electromagnetic counterparts. This difference in shape is an important way to differentiate the two, although complete differentiation is not always possible.

Figure 2.5 shows a Monte Carlo simulation of an air shower produced by a photon in contrast with one produced by a proton. The hadronic shower has a larger lateral spread than the more compact electromagnetic shower.

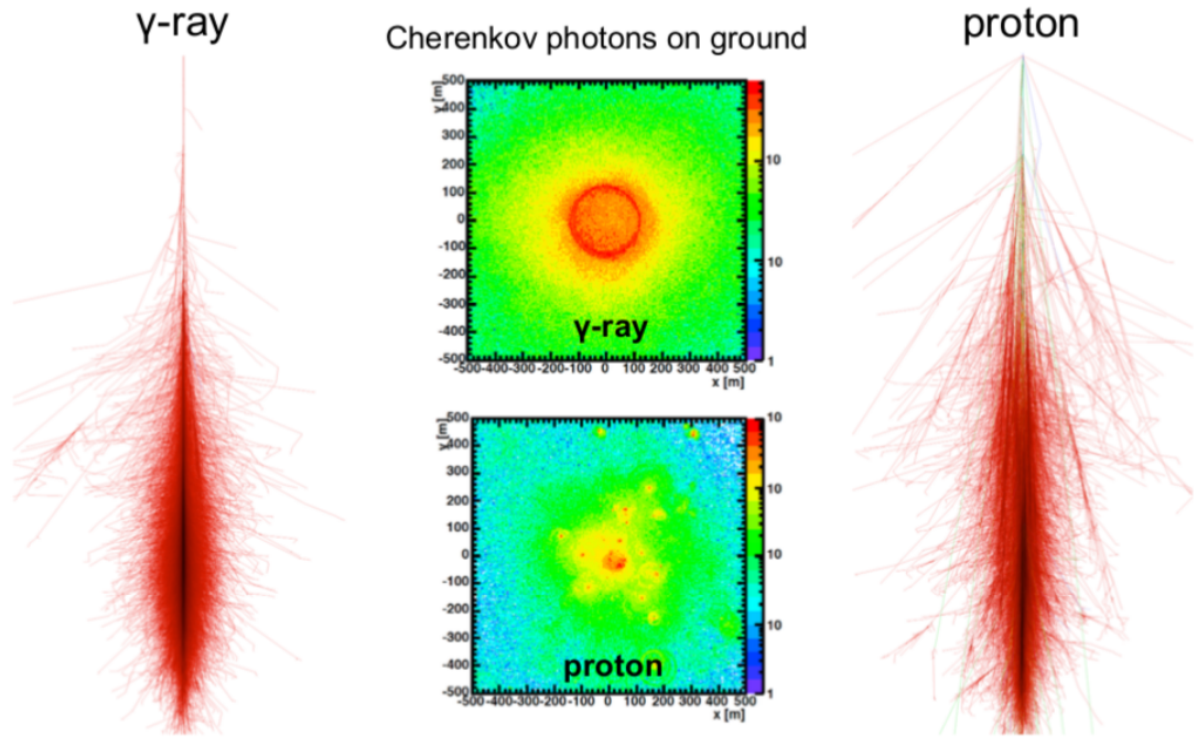


Figure 2.5: Monte Carlo simulations of 100 GeV gamma-ray (left) and cosmic-ray (right) air showers generated with the CORSIKA package ([Heck et al., 1998]). Image from [Petrashyk, 2019].

2.2 VERITAS Instrumentation

2.2.1 General Design

VERITAS, the Very Energetic Radiation Imaging Telescope Array System, comprises four telescopes of similar design. They are each constructed with a reflector, a camera box held on quadrupod arms, and a counter weight (see Figure 2.6). The telescopes are arranged in an approximately diamond formation (see Figure 2.7), with sides of about 100m. This distance was chosen to optimize the array's collection area, while always ensuring that more than one telescope is located in an air shower's Cherenkov light pool.



Figure 2.6: Photo of the VERITAS array. [Tsen-Yuan Lin, 2020]



Figure 2.7: Overhead view of VERITAS. Map data from Google (2015), markings by Tsen-Yuan Lin [2020]

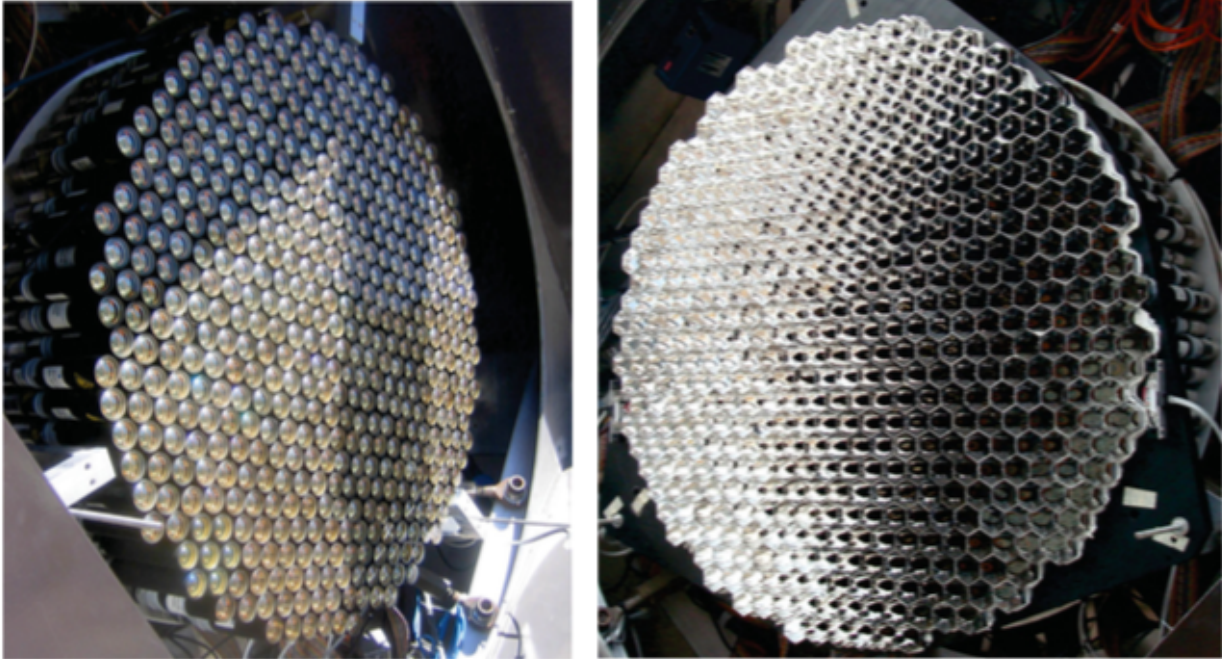


Figure 2.8: The VERITAS camera. Left: The camera without the Winston cones. Right: The Winston cones minimize the gaps between the PMTs. [Tsen-Yuan Lin, 2020]

VERITAS's reflectors are 12m diameter structures that follow the Davies-Cotton design [Davies, 1957]. Each steel structure supports 345 hexagonal tessellated mirror facets, with triangular suspension mounts that ensure the mirrors can be individually adjusted, and thus, properly aligned. With a curvature radius of around 24m, the reflector's focal length is about 12m.

Each VERITAS camera, situated at the focal point of a detector, (see Figure 2.8) is a pixelated photon detector consisting of 499 Hamamatsu photo-multiplier-tubes (PMT) arranged in a hexagonal pattern. PMTs are glass vacuum tubes whose inner fronts are coated with a photocathode material, a light-sensitive metal that converts photons into electrons via the photoelectric effect. This allows the transformation from photons hitting the PMT into an electric signal. This signal is then amplified as the electrons go through a chain of dynodes, generating more free electrons with every impact.

The VERITAS camera PMTs have a 20-30% photon detection efficiency, response times of a few nanoseconds, large detection areas with clean signal amplification, and can detect individual photons. They have a circular radius of 28.6 mm on the front face, which leaves gaps on the focal plane, but these are recovered in Winston cones (see Figure 2.8) [Winston, 1970]. These cones ensure that photons coming at an angle superior to 30° are not detected, which helps prevent light contamination. Each PMT "sees" 0.15° of the sky, resulting in a total VERITAS field of view of 3.5° .

2.2.2 Trigger System

After the photons are converted to an electric signal via the PMTs, the signal for each PMT is digitised continuously with a flash analog-to-digital-converter (FADC), and stored temporarily in a buffer. Because not all the data needs to be stored, VERITAS selects which events to store with a three-level trigger system.

The first trigger (L1) is at the pixel (PMT) level. For this level to be triggered, the signal from a PMT must exceed a defined threshold. The L1 triggers are important to keep out environmental background light, such as the night sky background, and electronic noise. They are implemented via constant fraction discriminators (CFDs), which stabilise the trigger timing and ensure it is independent of the PMT pulse-shape. If a pixel is triggered, the information is passed on to the second level.

The second trigger, L2, is at the level of an individual telescope. It necessitates that an adjustable number of neighbouring PMTs (usually 3, but can be raised up to 5) pass the L1 level simultaneously (that is, within a 6ns time window). This reduces the impact of random noise and background. If a telescope is marked as triggered at the L2 level, the only test left is L3. The L2 trigger has a time window of 8 nanoseconds (the maximum time span of a Cherenkov light pulse), and it is typically triggered at frequencies of a few kHz.

Finally, the L3 trigger is at the array level. It simply requires that a certain number of telescopes (usually two, but that number can be adjusted if needed) trigger at the L2 level. If that condition is passed, the read-out of the FADC samples for all PMTs and all telescopes is initiated in the buffer, and an event is built. L3 triggers typically occur at rates around 300 Hz.

Events that pass the L3 trigger are stored in Veritas Bank Format (VBF) files, which are then ready to be analysed. The VERITAS analysis is described in the following chapter.

Chapter 3

BL Lacertae Analysis

3.1 Analysis Tools

3.1.1 VERITAS Standard Analysis

In this section, I review the steps of the VERITAS standard analysis for gamma-ray data, specifically using EventDisplay [Maier and Holder, 2017], one of two main software packages used by the VERITAS collaboration. Written in C++, EventDisplay uses the data analysis routines of the scientific software framework ROOT [Brun and Rademakers, 1996] and is freely available upon request to Maier and Holder [2017].

Starting with a raw data file, this analysis asks whether there is a gamma-ray source, and if so, reconstructs the properties of the gamma-ray source — notably, its location, flux evolution, and energy spectrum.

Charge Integration In each pixel (that is, each PMT), the total charge is calculated by integrating the FADC trace over a time window. When the PMTs encounter Cherenkov photons, a typical signal is similar to that on the left of Figure 3.1: a rapid dip, followed by a slower rise to the baseline value (or pedestal). T_0 is defined as the signal’s arrival time, when the trace reaches half its minimum value. On the right of Figure 3.1, we see

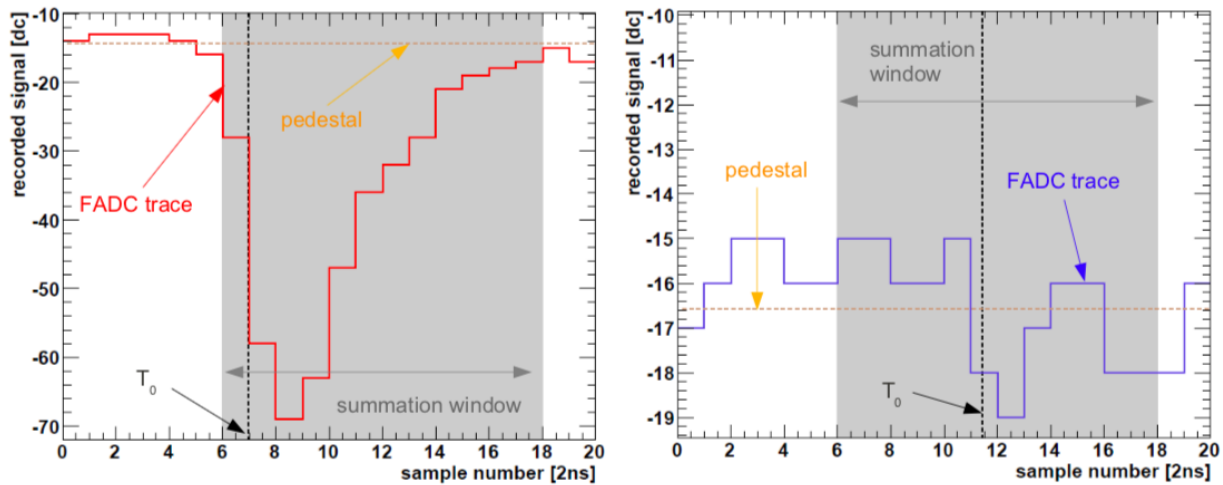


Figure 3.1: Two typical FADC traces. Left: Trace from one channel that has received a significant Cherenkov photon signal. In grey, a 12 sample (24 ns) time window over which the trace of the FADC was integrated. The trace is offset from 0 by a pedestal of approximately 16 digital counts (dc), marked by an orange dashed line. Right: Without a Cherenkov signal, the FADC trace fluctuates around the pedestal. Figure from Krause [2017].

what the FADC trace typically looks like when no Cherenkov photon signal is detected: it fluctuates around the pedestal value.

The EventDisplay package uses a double-pass approach for charge integration [Holder, 2005]. The FADC trace is first integrated over a wide time window (16 ns or longer), after which follow the steps of cleaning and parametrisation described below, and T_0 is calculated. Afterwards, the charge is integrated again, this time over a smaller time window (typically 12 ns) to get a better signal-to-noise ratio. The boundaries of this small time window are determined by fitting the temporal shower development over the image’s major axis — the slope of this fitted function determines the start of the integration interval. Finally, we subtract the pedestal value and obtain the total charge in digital counts.

To calibrate data, VERITAS takes artificially triggered runs every night, where the camera is uniformly illuminated by LEDs or laser flashes. By analyzing these flash runs, we

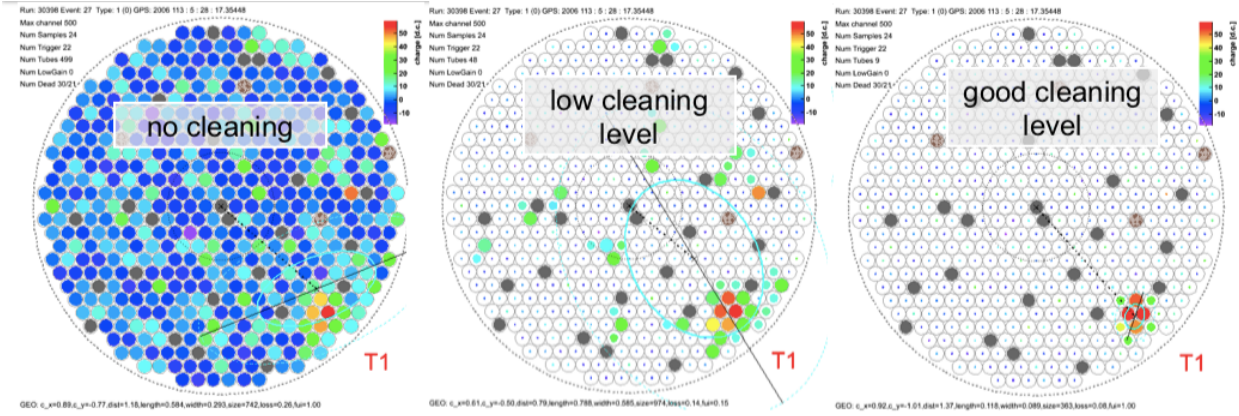


Figure 3.2: Pixel (PMT) information before and after cleaning. Color proportional to charge (i.e. pixel brightness), with blue for low towards red for high. Grey indicates dead pixels, white, pixels that were excluded by cleaning. Figure from Maier [2014].

can calculate the PMTs' relative gains, timing differences, and estimate the pedestal value in each FADC trace and the background noise coming from the night sky.

Image Cleaning To remove random background fluctuations (for example, due to the night sky background), the image is "cleaned". The pedestal variance (pedvar), calculated as the root-mean-square of the pedestal distribution, is an essential value for this process, since it depends on the brightness of the night-sky background on any given night. Pixels with a charge greater than 5 pedvar above the pedestal value are selected as *image pixels*. Then, pixels that have 2.5 pedvar above the pedestal value and are the neighbor to an image pixel are selected to become border pixels. Every other pixel is zeroed, including pixels that might have passed the 5 pedvar test but with no adjacent boundary pixels. This process is illustrated in Figure 3.2.

Image Parametrisation The recorded and cleaned shower image is now assigned a set of Hillas parameters that define its shape and orientation. These parameters are fitted through a moments analysis as described in Hillas [1985], and the process takes advantage of the fact that shower images will be elliptical and of stronger intensity at the centre. From there, the obtained parameters are the number of pixels N_{pix} , the size s (total light

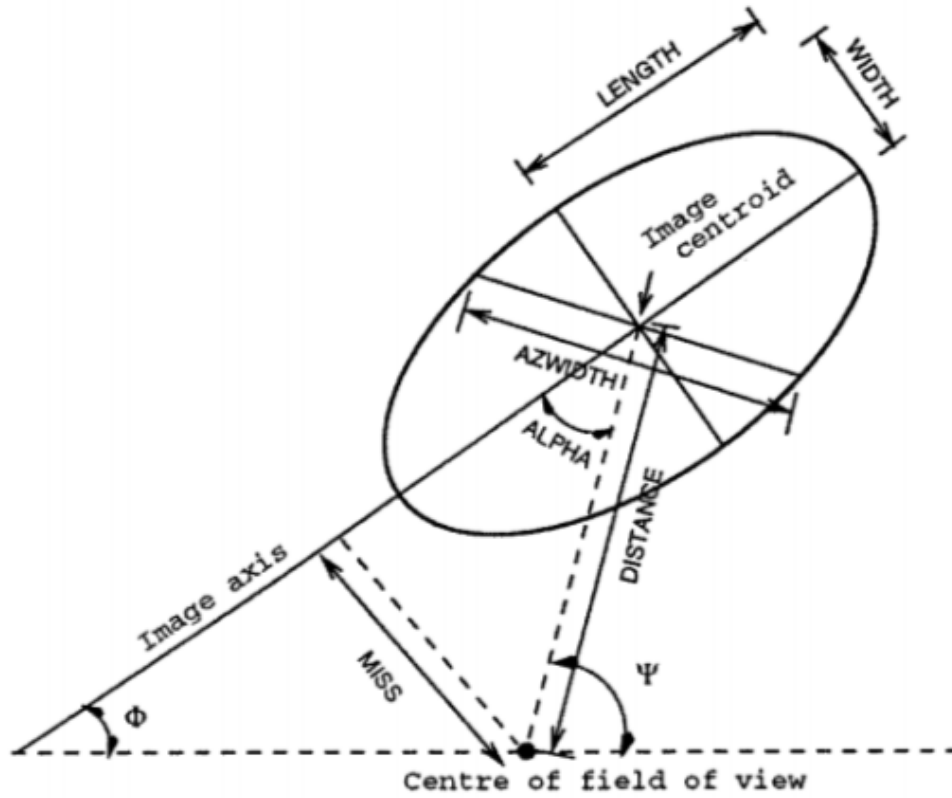


Figure 3.3: Hillas parameterization of shower images. Figure from Fegan [1997].

intensity in the image), the width (minor axis) and length (major axis) of the shower ellipse, and the distance from the center of the ellipse to the center of the camera (Figure 3.3).

These parameters can be used to make cuts based on image quality (for example, if too much of the image is at the edge of the camera), resulting in better resolution. Quality cuts include for instance minimum image size ($s > 400$ dc), and a minimum of boundary/image pixels ($N_{pix} \geq 5$). [Krause, 2017]

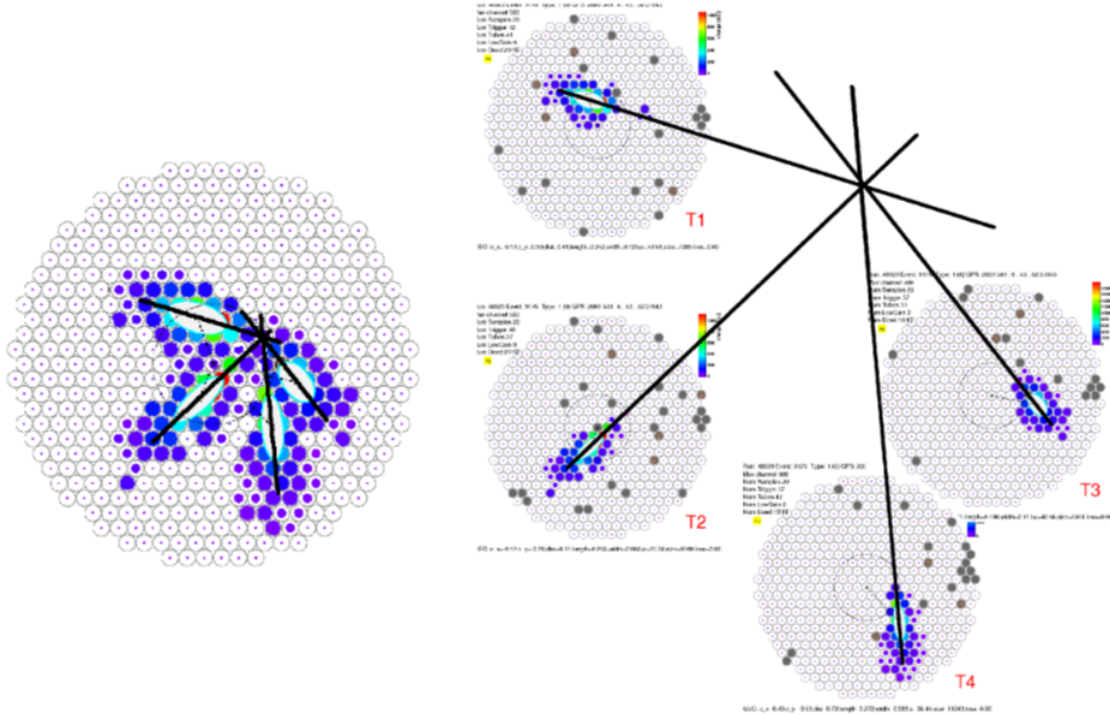


Figure 3.4: Examples of geometrical reconstruction. Left: Reconstruction of direction. Right: Reconstruction of the shower core location. Figure from Petrashyk [2019]

From these images and parameters, we would like to reconstruct the direction of the primary gamma ray and its energy. The next paragraphs detail how these values are obtained.

Geometrical Reconstruction One of the most important parameters to reconstruct is the original direction of the gamma-ray, since this tells us where the source is located in the sky. Fortunately, air showers develop along the axis of the initial particle direction (see section 2.1), such that the origin of the shower is located on the image ellipse’s major axis. The reconstruction of the event direction is done by following algorithm 1 of Hofmann et al. [1999], where several independent shower images from different telescopes are stacked on a single camera plane (see Figure 3.4, left). The point where the major axes intersect for each pair of ellipses is measured, and we take the weighted average of the intersection points. The weights are calculated from the angles between the image axes, the

image size, and the width/length ratio, in order to attribute higher weights to brighter, more elongated images.

A related geometrical parameter to determine is the position of the shower core on the ground, i.e. the location where the gamma-ray would have landed if it had passed through the atmosphere unimpeded (see Figure 3.4, right). By projecting the image axes onto a plane normal to the telescope's pointing direction, we look at the straight line where the planes intersect the ground. The shower core must be located on that line. To calculate its position, we minimize the distances from the major axes to the source. This allows us to determine the impact parameters, defined as the distances between the telescopes and the shower core. The impact parameter is important to help estimate the energy of the primary particle, as will be described in the next section.

Lastly, we want to estimate the emission height h_{em} of the Cherenkov emission. For each pair of telescopes, h_{em} is estimated, and the final estimate is the mean of these pairs weighed by image size. The χ^2 value of h_{em} is also important, and both of these values are helpful to separate gamma-ray showers from hadronic showers (since charged CRs and muons penetrate deeper into the atmosphere).

Energy Reconstruction Finally, we want to extract the energy E_0 of the primary particle from the shower images, which will be key to measuring the energy spectra of VHE sources. The total charge captured by the camera pixels, s , is proportional to the number of Cherenkov photons produced during the air shower, which itself depends on E_0 , and can thus be used to reconstruct it. We must also take into account other parameters that influence s : the shower direction, impact parameter, background noise level, and zenith and azimuth angles (i.e., pointing direction).

Monte-Carlo (MC) simulations of gamma-ray air showers using the CORSIKA package [Heck et al., 1998] are an important part of the VERITAS analysis. They are used

to produce lookup tables, where for a wide range of zenith angles, wobble offsets¹, and night sky background levels, the energy E_0 is calculated as a function of measured impact parameter R and total charge s , as well as the energy median E_{med} , and the 90%-width σ_i^E .

An energy estimate E_i is calculated for each telescope image. Because the MC simulations are done for finite values of zenith angles, wobble, and noise, E_i is estimated by interpolating between discrete steps. The reconstructed E_0 is then obtained by computing the average of E_i over N telescopes over the 90%-width σ_E :

$$E_0 = \frac{\sum_{i=1}^N E_i / (\sigma_i^E)^2}{\sum_{i=1}^N 1 / (\sigma_i^E)^2} \quad (3.1)$$

And the χ^2 distribution of this energy estimate is:

$$\chi_E^2 = \frac{1}{N-1} \sum_{i=1}^N \left(\frac{E_0 - E_i}{(\sigma_i^E)^2} \right) \quad (3.2)$$

3.1.2 Boosted Decision Trees for Gamma/Hadron separation

As was alluded to in section 2.1, one of the main challenges for gamma-ray astronomy is to differentiate between air-showers induced by VHE photons, and those caused by hadrons. Separating the gamma-ray signal from the hadronic background is essential to achieve high sensitivity. This is especially important for BL Lac in the quiescent state, since we're analyzing faint data. In this section, I will go over the technique of cuts that was traditionally used in the VERITAS analysis, then the method of Boosted Decision Trees first developed by Krause et al. [2017], which was used to analyse BL Lac in the quiescent state.

¹The wobble observation technique is the practice of pointing at a position deliberately offset from the targeted source in order to estimate background and observe the target simultaneously. VERITAS observations typically wobble 0.5° around a source, alternating between North, South, East, and West wobbles. Recall that the VERITAS field of view is 3.5° .

Standard Cuts One of the key differences between air showers caused by gamma rays and by hadrons is in their shapes. Hadronic showers are messier, more irregular, and wider (see section 2.1.2). For that reason, an intuitive way to separate them is to calculate the Hillas widths and lengths. MC values for gamma-rays are stored in lookup tables as a function of size and impact parameter, and can then be used to calculate the mean scaled width (MSCW) and mean scaled length (MSCL) of observational data:

$$MSCW = \frac{1}{N} \sum_{i=1}^N \left(\frac{w_i - \omega_{MC}(R, s)}{\sigma_{w,MC}(R, s)} \right) \quad (3.3)$$

$$MSCL = \frac{1}{N} \sum_{i=1}^N \left(\frac{l_i - \omega_{MC}(R, s)}{\sigma_{l,MC}(R, s)} \right), \quad (3.4)$$

where l_i is the length, w_i is the width, N is the number of images, ω_{MC} is the median of the width/length found in look-up tables, σ is the 90 %-width values of the expected image width, also found in look-up tables, R is the impact parameter, and s is the image size. By construction, mean-scaled quantity distributions for gamma-rays should be centred at zero and have a width of ~ 1 .

Cut-values for these parameters are chosen based on MC simulations of air showers, and events which do not meet the required criteria are removed. Though this process is effective, it is limited to shape parameters and will inevitably lead to some background being categorized as signal, and vice-versa. A perfect separation of background and signal is impossible, but the effectiveness of the separation can be improved by considering a multivariate approach such as Boosted Decision Trees that takes into account other potentially discriminating parameters.

Decision Trees Decision Trees are a multivariate method of classification. By classification, we mean that the algorithm's output is a category — in this case, whether an event is "signal" or "background". A multivariate analysis considers several variables at the same

time, even while their correlations may be non-linear. For hadron/gamma separation, the VERITAS analysis considers the following variables:

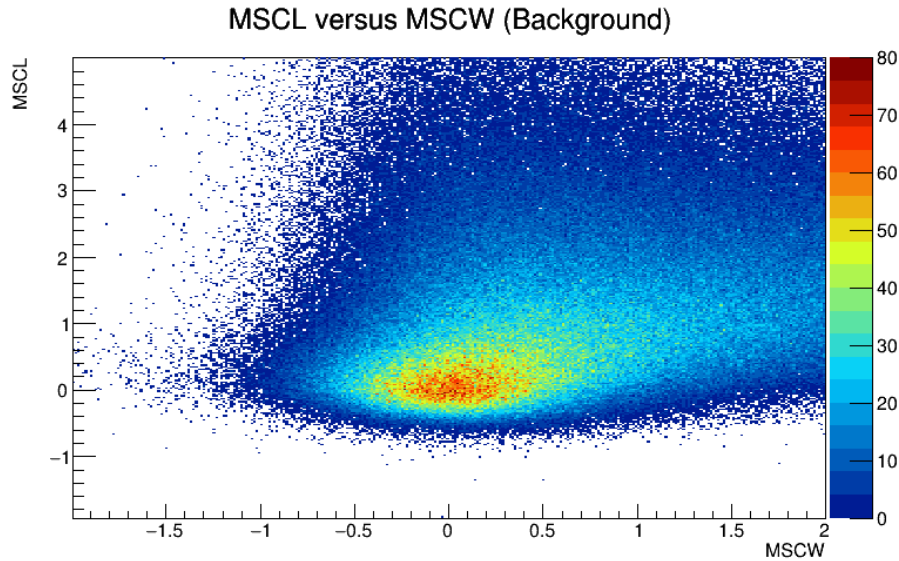


Figure 3.5: Distribution of mean-scaled width vs mean-scaled length for a background training sample (real data taken on a patch of dark sky).

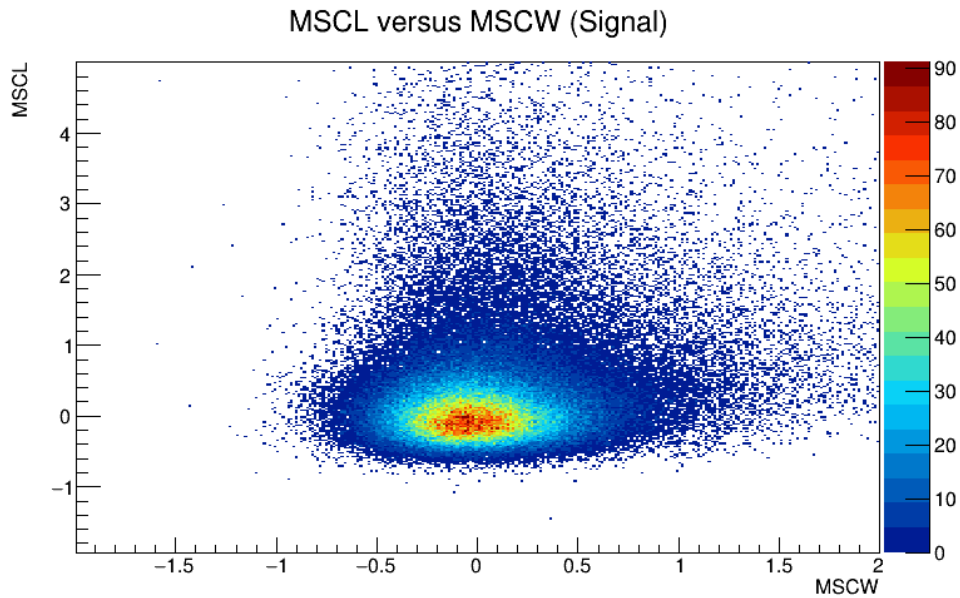


Figure 3.6: Distribution of mean-scaled width vs mean-scaled length for a signal training sample (Monte-Carlo simulation of gamma-ray data).

- Shape parameters (MSCW, MSCL) as described earlier (see Figures 3.5 and 3.6).

- Height of maximum emission, particularly relevant at low energies or high zenith angles (see Figure 3.7).
- χ^2 -value of the emission height estimation (see Figure 3.8).
- Second largest image's size in photoelectrons (see Figure 3.9).
- Distance from shower core (see Figure 3.10).

Figures 3.5-3.10 show the distribution of these variables on a training sample for one energy/zenith bin. The "background" comes from real data of patches of the night sky with no sources (thus, primarily charged cosmic rays), whereas the "signal" sample is a Monte-Carlo simulation of gamma-ray showers. From these distributions, the difference between the two populations is visible, but it is obvious that a simple cut based on one or more of these parameters will result in important losses of signal and/or gains in background noise.

These distributions are influenced by energy and zenith angle, as can be seen in Figure 3.11.

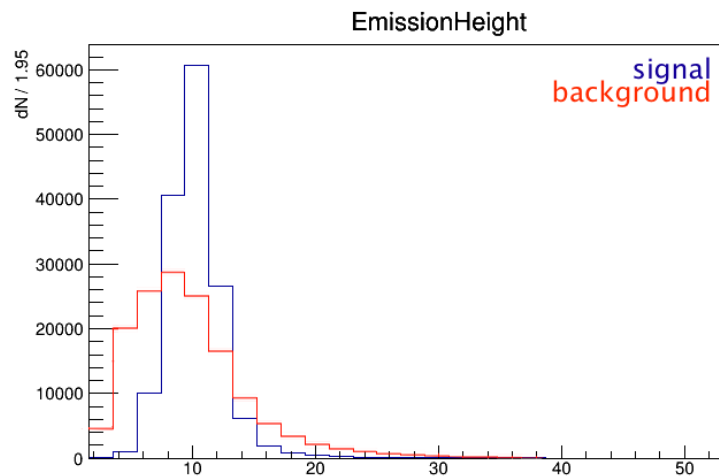


Figure 3.7: Distribution of shower emission height for a background training sample (data) vs signal (simulation).

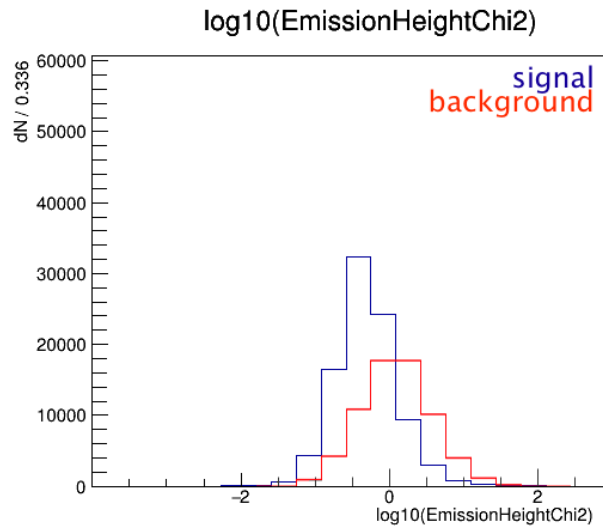


Figure 3.8: Distribution of the χ^2 of shower emission height for a background training sample (data) vs signal (simulation).

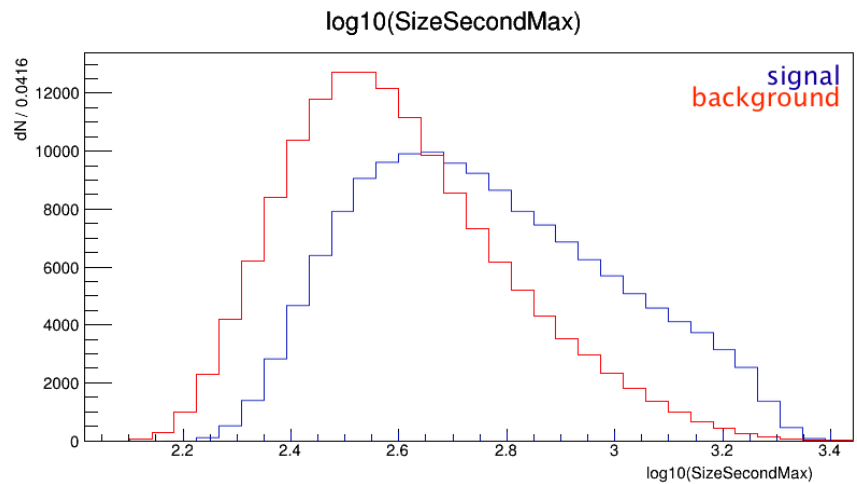


Figure 3.9: Distribution of the second largest image's size for a background training sample (data) vs signal (simulation).

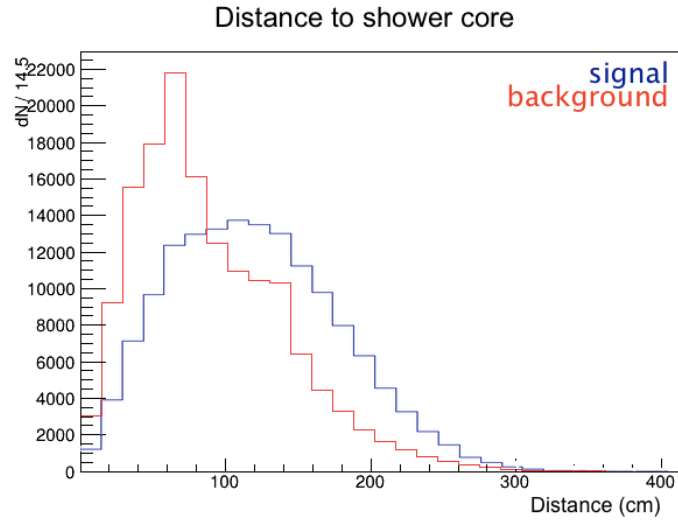


Figure 3.10: Distribution of the distance to shower core for a background training sample (data) vs signal (simulation)

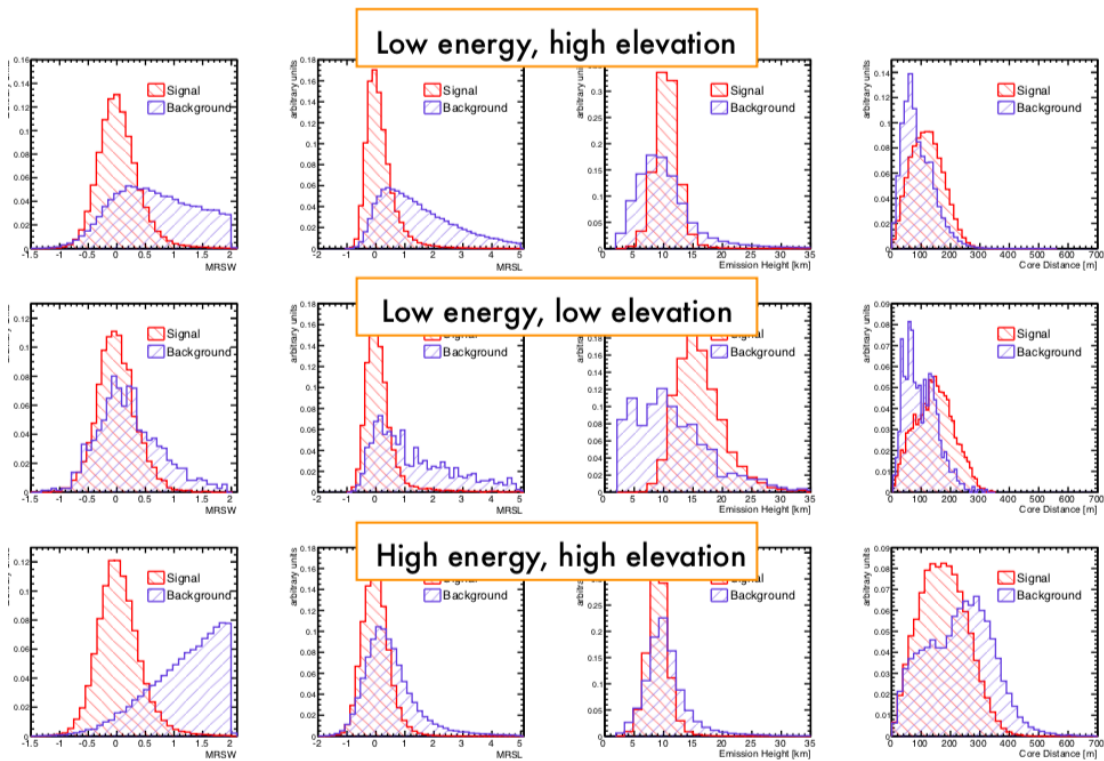


Figure 3.11: Examples of how energy and zenith angle affect the distribution of discriminating variables, from left to right: MSCW, MSCL, emission height, core distance. For this reason, training of boosted decision trees must be done for separate zenith and energy bins. From Krause and Poeschel, 2017.

Figure 3.12 shows a visual representation of a decision tree. Decision trees are 2-D structures composed of nodes (the “branches”) and leaves (the final output). Mother nodes split into two daughter nodes with a splitting criterion which tells whether the event is more like a signal or like background. The event’s parameters pass a series of tests before being classified as signal or background (to a certain degree of probability). The best separation criterion for each node is defined during training, in which the tree is fed a data set of simulated events (whose types are thus known).

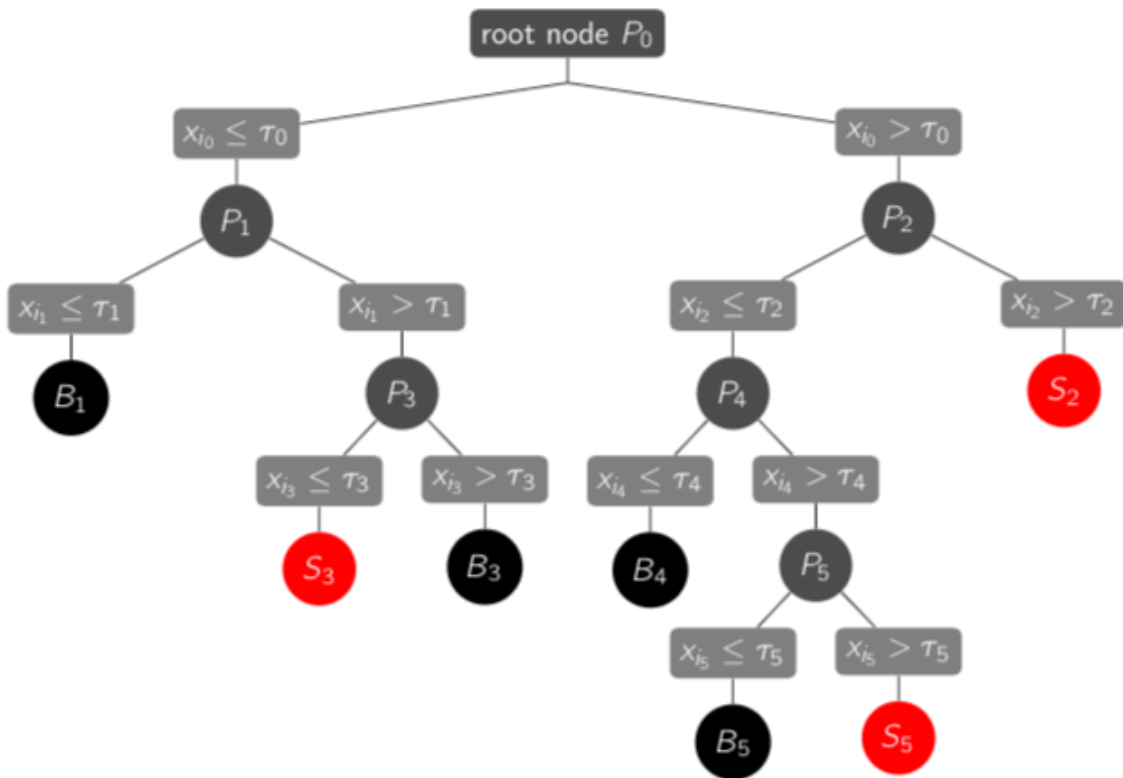


Figure 3.12: Visual representation of a decision tree’s development. An event with a set of parameters x_{ij} undergoes a series of binary criterion tests, until it reaches the final node, by which point it is categorized as signal (S) or background (B). From Krause [2017].

Training We first start at the root node with the entire training sample T , composed of a set of background (T_B) and signal (T_S) simulations. Each of the events in T have a set of parameters and a weight w_i (before boosting, which will be covered below, all weights

are equal). At each of the nodes, the training sample is split into leaf nodes according to an attribute. The criterion which splits the sample best is applied, and is found using the following index:

$$I = \left(\sum_{i=1}^N w_i \right) P \quad (3.5)$$

where N is the number of events in the sample and P measures the signal purity. It is equal to 0 when all events in the sample fall into the same category, and is at its maximum (0.25) when there are equal numbers of signal and background events. Maximizing the difference between the index of the mother node with the daughter nodes gives us a criterion C that splits the sample most efficiently.

$$Gain(\Delta I(C)) = I_{mother} - I_{right} - I_{left} \quad (3.6)$$

T is then split in two subsets: on one daughter node, the events which pass the criterion, and on the other, those which fail it. This process begins again with each node, until the splitting cannot be increased further. At that stage, the node becomes a leaf, one which is classified as signal if more than half of its events are gamma rays, and background if not.

Boosting Single decision trees are sensitive to the fluctuations of the training data set and can thus result in criteria that will only work with the training sample. Boosting can solve that problem. It extends a single tree to a forest, where each tree is more impervious to statistical fluctuations than the last.

We start with a training sample where each event has the same weight w_i^0 and build a tree T^0 . When an event μ is misclassified by the tree T^n , its weight will be boosted by a factor of α_{n+1} , such that:

$$w_{\mu}^{n+1} = w_{\mu}^n e^{\alpha_{n+1}} \quad (3.7)$$

And the other weights will be normalized. α_{n+1} is:

$$\alpha_{n+1} = \beta \ln \left(\frac{1 - \epsilon_n}{\epsilon_n} \right), \quad (3.8)$$

where ϵ_n is the weight fraction of misclassified events for t_n (sum of misclassified weights over the total sum of weights), and β is the (unitless) learning rate, which is adjustable by the user.

Following Krause et al. [2017], we use 400 trees, a maximum node depth of 5, 20000 signal training events (from simulation), 20000 background training events (can also be from simulation, but we usually use night sky background data). We first perform some standard cuts to exclude events that are obviously not gamma-ray, and the BDT analysis refines the separation.

To account for variations in energies and zenith angle (both of which will change the perceived shape of the air-shower), the BDTs are trained over four energy bins (0.08 TeV to 0.32 TeV, 0.32 TeV to 0.5 TeV, 0.5 TeV to 1 TeV, and >1 TeV) and four zenith angle bins (0° to 22.5° , 22.5° to 32.5° , 32.5° to 42.5° , and $>42.5^\circ$). This allows the bins to be fine enough that the variations are considered, while still including enough events for the training.

An important risk to bear in mind in any classification algorithm is overtraining, when the algorithm follows the training sample too closely and statistical fluctuations take over. This can happen, for example, when the tree depth is set too high. To avoid this, every BDT training is followed by an overtraining check. The training sample and a test sample are compared by a Kolmogorov-Smirnov test, which calculates the probability that the signal (and background) training and testing distributions come from the same probability function. If there is no overtraining, i.e. if the two come from the same probability function, then the test will give a non-zero probability result. A result close to zero signals overtraining.

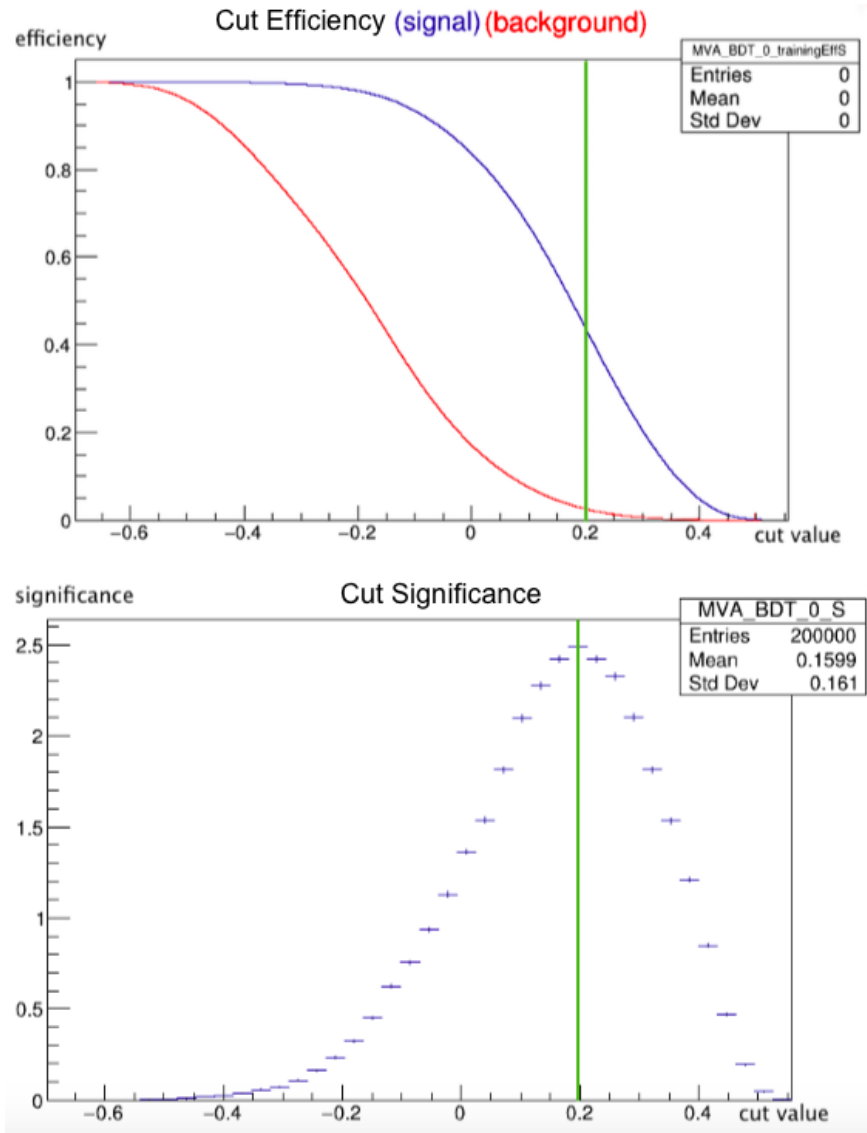


Figure 3.13: Upper: Efficiency of background (red) and signal (blue) as a function of cut value. The green line represents the optimal cut value. Lower: signal significance as a function of cut value. The green line is the optimal cut value. We see that it is the extremum of the significance curve.

Cut Optimization Finally, the BDTs' output is a "score" between -1 and 1. We need to choose a threshold for that score such that all events underneath it are deemed background, and the rest, signal. Figure 3.13 shows an optimized cut value. The process of finding the best threshold for this score is called cut optimization. By best, we mean

the cut that will minimize the minimum signal strength that can be detected for a given background.

These cuts are determined for every zenith and energy bin, and are optimized in three ways that are better suited for sources of varying strength and spectral index: soft, moderate, and hard. Soft cuts are typically used for sources with a spectral index ≥ 3 , which are best served by low size cuts. They have a low energy threshold, but they also have a lower signal-to-noise-ratio. Hard cuts, on the other hand, are best for sources with harder spectral index (≤ 2) or weaker sources. These cuts result in a smaller point-spread function and better signal-to-noise ratio, but their energy threshold is higher, so they are not as suited for lower energy gamma-rays [Park, 2016]. Moderate cuts are, intuitively, a compromise between the two and can be used for most sources.

3.1.3 Bayesian Block Analysis

The method of Bayesian Blocks was first invented by Scargle [1998], then was generalized and improved in Scargle et al. [2013]. Its purpose is to detect local variability in sequential data in a more unbiased way than simply by eye. It aims to identify and characterize variations of statistical significance while taking into account observational errors. The sought structures are local, meaning that the variations occupy sub-ranges of the total time interval considered (as opposed to global features such as periodicities which would be better detected by, for example, a Fourier transformation). In this work, a Bayesian Block analysis was used to identify which parts of the BL Lacertae light-curve (flux as a function of time) should be classified as "flaring" or "quiescent" (see section 3.2.2). I will now give a brief overview of Bayesian Blocks.

One of the strengths of the Bayesian Blocks method is that it is a non-parametric approach, meaning that it searches for a generic representation. It does not make any assumptions about the smoothness or shape of the signal.

We are looking to divide a light-curve in time intervals that represent a quiescent state and one or more flaring states. One of the best ways to go about this is to fit a piecewise-constant model to the data optimally. This is a type of change-point analysis, that is, one that seeks points where the signal discontinuously changes from one segment in which the data is constant (to a certain level of statistical certainty) to another. It is an ideal approach for discrete, sequential, one-dimensional data. The piecewise-constant model divides the independent variable (here, time) into subintervals called "blocks" of (generally) unequal size. Within the blocks, the dependent variable (here, brightness) is modelled as a constant within errors. Scargle et al. [2013] found that this approach was the best step-function to maximise the quality of the fit.

Importantly, the blocks can be treated as independent of each other. The fitness of a block is only dependent on the data within the block. By using a Bayesian likelihood framework, we can thus compute a fitness function with only two parameters: the block's width, and the signal amplitude.

The idea is then to vary the location of the change-points to achieve maximum fitness. However, this is challenging when the number of points N is large, since the number of possible block configurations would be 2^N . Instead of calculating all of these possibilities, a dynamic programming approach will be much more efficient.

Dynamic programming is the practice of reducing the complexity of a problem by reducing it into smaller, more manageable sub-problems dealt with recursively. In this case, it can be seen as akin to mathematical proof by induction (proving a proposition for a starting point 0, then proving that if this proposition is true for n , it is true for $n+1$). It is easy to determine the best binning for a single data cell. Then, Scargle et al. [2013] showed that by defining the step between optimal binning for n cells to $n+1$ cells, and reusing the results stored from previous steps, computation time is reduced to the order of N^2 , which

is a much less daunting number for large N . The recursive nature of the algorithm allows it to stop analysing whenever a change-point is detected.

More mathematical details about Bayesian Blocks and their implementations can be found in Scargle et al. [2013]. In this work, I've made use of astropy's bayesian block algorithm [Astropy Collaboration et al., 2018], based on the Scargle algorithm.

3.2 Analysis Results

3.2.1 Full archival data set and quality cuts

Over VERITAS's decade of activity, BL Lac has been observed for hundred of hours. The first step in determining whether BL Lac is detectable in the quiescent state was to gather all that archival data and apply some quality cuts. VERITAS observers classify the weather on a letter scale, where A-weather defines a clear sky that requires no time cut. On the other hand, B-weather and C-weather nights, which correspond to cloudy or otherwise unclear skies, sometimes still have usable data, but they need to be checked for potential cuts. Changes to the L3 trigger (array-level) rate and temperature of the sky measured by an infrared radiometer are good indications of when an obstruction (such as a cloud) occurred, and when a time-cut should be applied. See Figure 3.14.

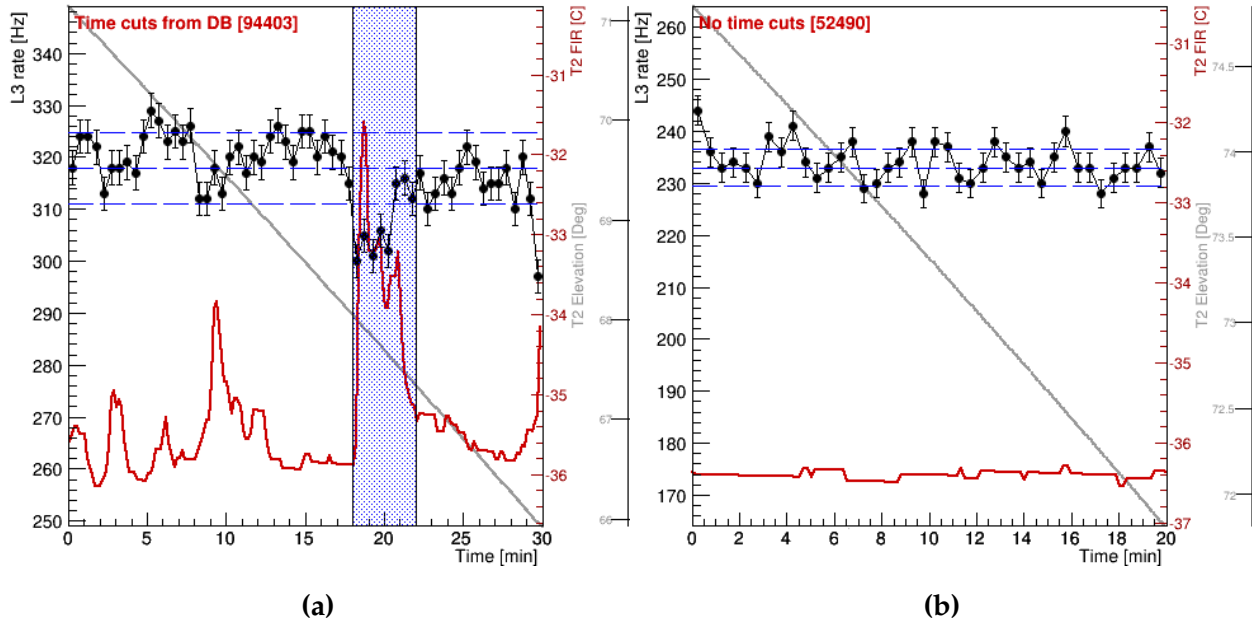


Figure 3.14: Two contrasting examples of L3 rate that do and do not require time cuts. In black, the L3 trigger rate. In red, the infrared radiometer (FIR) temperature. (a) An example of data that require a time-cut (in blue). The sharp spike in the FIR temperature along with the dip in L3 rate usually indicate the passage of a cloud or another obstructing weather event. (b) Example of data that do not require a time cut. Both the L3 rate and FIR temperature are stable.

Once those cuts were applied, the BL Lac data set analysed in this work comprised 271 runs, for a total of over 99 hours of data, spread over 11 years (see table 4.1.). The date of each run was an important factor to take into account in the analysis, since the instrument has changed over that decade. Three major epochs mark before and after the telescope T1 was moved in 2009, and before and after the PMTs were upgraded in 2012. In addition to that, the aging of the instrument affects the data taken, so the epochs must be sliced into finer year-long intervals. Finally, the data is also calibrated based on how the atmosphere changes with the seasons (summer and winter). This leads to different look-up tables being used to reconstruct effective area, energy, and geometry.

The data was analyzed with EventDisplay (see section 3.1.1). The gamma-hadron separation was performed using Boosted Decision Trees soft cuts (see section 3.1.2).

Number of Runs	271
Exposure	99 hours
Mean elevation	68.4°
Trigger rate	107.2 Hz
mean pedvars	6.41 digital counts

Table 3.1: Properties of the total BL Lac data set.

The final resulting lightcurve can be seen in Figure 3.15, with night-by-night time bins. The obtained significance skymap is showed in Figure 3.16. With a rate of 0.48 ± 0.01 gammas/min, we have a clear detection with a significance of 44.4σ at the source location, which was expected. As seen in Figure 3.15, the data set comprises clear flares. Our next question is then whether BL Lac can also be detected by VERITAS when it is not flaring.

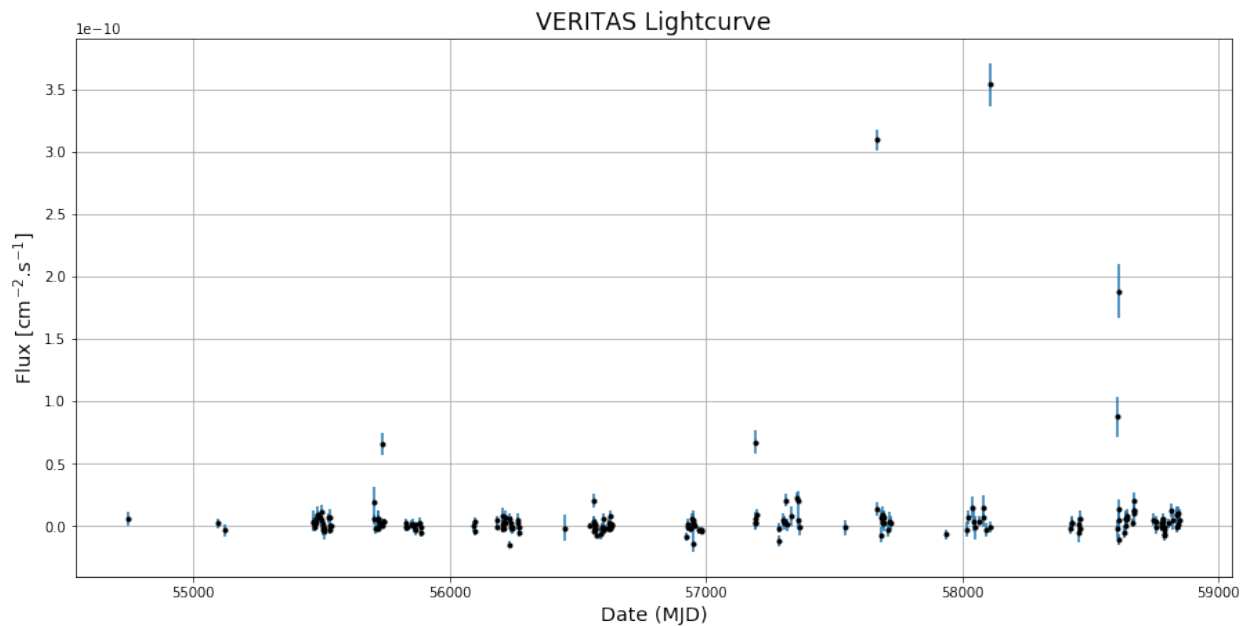


Figure 3.15: The lightcurve of BL Lac over 11 years of data, binned nightly.

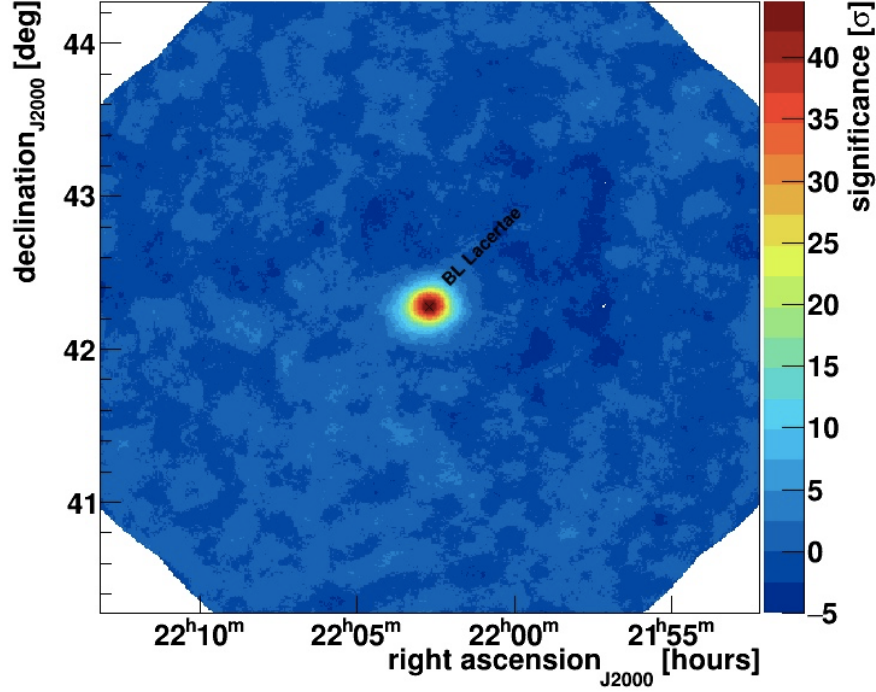


Figure 3.16: Smoothed significance skymap of the full data set of BL Lac. The maximum significance occurs at the source location, at 44.4σ .

3.2.2 Identifying Flares

To identify on which nights BL Lac should be marked as flaring, we perform a Bayesian Block analysis as described in 3.1.3. The significance of each block was chosen to be 3σ , and the Bayesian Block package used was that in Astropy [Astropy Collaboration et al., 2018]. The resulting partition is shown in Figure 3.17. Taking into account each point’s uncertainty, the lightcurve is sorted into 11 blocks: six of them are long, spanning years and with a low average flux, and five blocks that are one-night long² and of a much higher flux than the average. The former blocks are defined as BL Lac’s quiescent state; the latter, as flares.

²The third flaring bin includes two nights. However, we can see that the first night’s flux is close to zero, and that months separate it from the next data point. This is an occasion when the Bayesian Block analysis should not be trusted blindly. Most likely, the sparsity of the data around that time caused this anomaly, and we do not consider the first night as part of the flare.

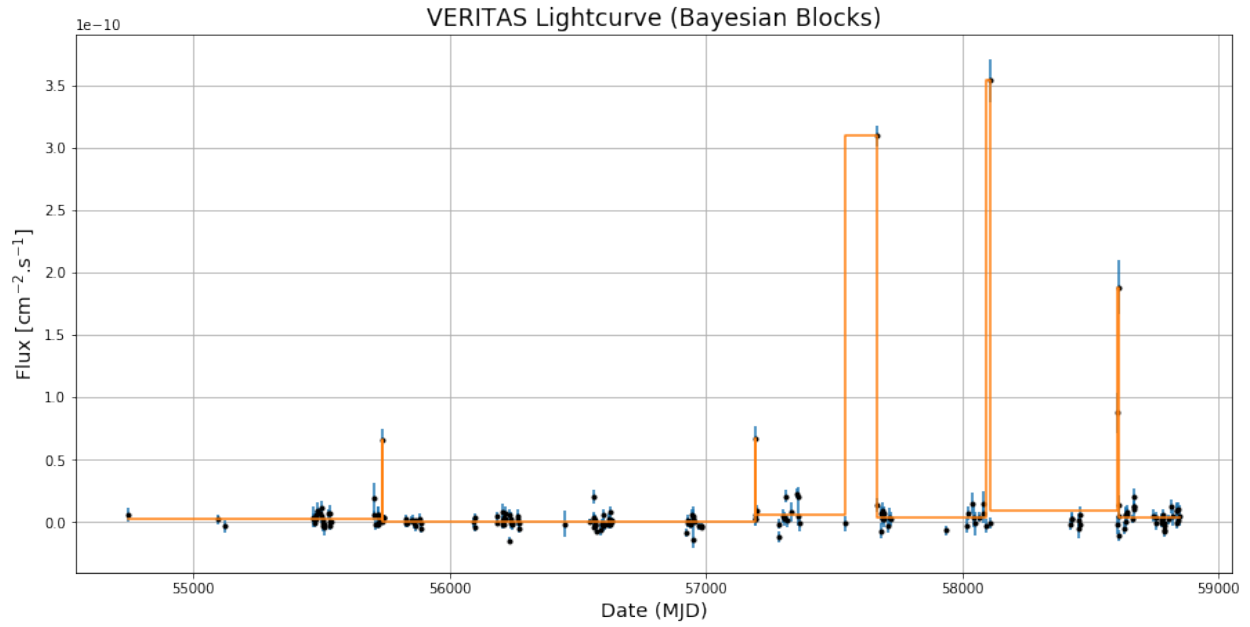


Figure 3.17: Light curve of BL Lac, with the Bayesian Block edges shown in orange.

Table 4.2 shows the flaring dates that were identified with this analysis: in 2011, 2015, 2016, 2017 and 2019. Overall, the flares consist of over 6 hours of data.

Date	Significance of Individual Runs	Event Rate (γ/min)
2011 June 28	13 σ	2.7 \pm 0.3
	3.1 σ	0.31 \pm 0.1
	0.2 σ	0.046 \pm 0.294
2015 June 20	8.7 σ	1.1 \pm 0.2
	4.9 σ	0.77 \pm 0.25
2016 October 5	22 σ	6.0 \pm 0.5
	25 σ	7.1 \pm 0.4
	24 σ	8.6 \pm 0.6
	27 σ	8.5 \pm 0.5
	28 σ	8.6 \pm 0.5
	15 σ	3.0 \pm 0.3
2017 December 20	14 σ	3.4 \pm 0.3
	19 σ	3.3 \pm 0.3
2019 May 5	11 σ	1.6 \pm 0.2

Table 3.2: Flares as determined by the Bayesian Block analysis. Each line is one VERITAS run (typically around 30 minutes long).

3.2.3 BL Lac in the quiescent state

Now that we have identified the flares, we can exclude them and analyse the quiescent data alone. The non-flare data consists of 93 hours of exposure, or 257 runs. The quiescent data set is 15 times longer than the flaring data, but the flares are still far more significant, highlighting the extreme variability of the source.

Figure 3.18 shows the significance skymap for the quiescent data. The maximum significance at the source location is 4.3 σ — not rising to the 5 σ often used in the literature

to claim a discovery of a previously unknown source, but significant enough to argue that BL Lac does indeed emit TeV gamma-rays when it is in its quiescent state.

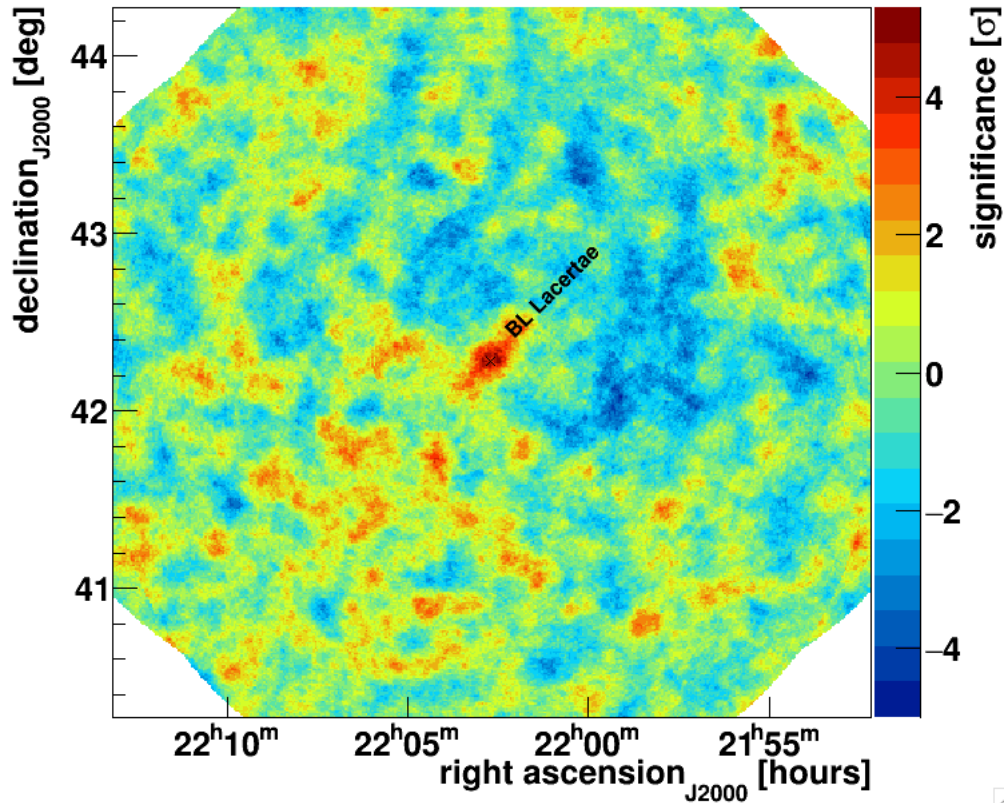


Figure 3.18: Smoothed significance skymap of BL Lac in the quiescent state. The maximum significance of 4.3σ is obtained at the location of BL Lac.

Another interesting question to consider is whether the spectral behavior of BL Lac is any different between the quiescent and flaring states. To do so, we first reconstruct the spectrum for only when the source is flaring and compare it to the quiescent spectrum (see Figure 3.19).

To obtain these energy spectra, the VERITAS analysis uses look-up tables (based on simulation data), and the unfolding method of correction factors Cowan [1998]. The idea of this method is to assume that the true value of the flux can be related to the measured

flux in each bin with a correction factor C_i :

$$\hat{\mu}_i = C_i \nu_i \quad (3.9)$$

Where μ_i is the true flux value, and ν_i is the measured flux value. C can be estimated with a Monte-Carlo simulation that assumes the shape of the true distribution to estimate μ_i^{MC} and considers the properties of the instrument for the resulting "observed" ν_i^{MC} :

$$C_i \approx \frac{\mu_i^{MC}}{\nu_i^{MC}} \quad (3.10)$$

Then, C_i and the measured ν_i can be used to estimate the true flux.

The points are then fitted to a power-law:

$$\frac{dN}{dE} = I \times \left(\frac{E}{1TeV} \right)^{-\Gamma} \quad (3.11)$$

For the non-flaring spectrum (see Figure 3.19), we obtain a factor I of:

$$I_Q = (1.8 \pm 0.7) \times 10^{-13} cm^{-2} s^{-1} TeV^{-1} \quad (3.12)$$

And a spectral index Γ of:

$$\Gamma_Q = 2.6 \pm 0.7 \quad (3.13)$$

The spectral index is especially important to compare to models of energy emission. Unfortunately, even 93h of data results in a soft detection, so we find a spectral index with a large uncertainty. For the spectrum in the flaring state (see Figure 3.19), the best fit we obtain is:

$$I_F = (1.92 \pm 0.08) \times 10^{-11} cm^{-2} s^{-1} TeV^{-1} \quad (3.14)$$

$$\Gamma_F = 3.15 \pm 0.04 \quad (3.15)$$

Thus, while the quiescent energy spectrum appears to be harder than the flaring energy spectrum, the spectral indices are consistent within our uncertainties (see Figure 3.19). This is an interesting and surprising result, as typically, HBLs have a “harder when brighter” behavior, i.e. their spectral index is *harder* when the source is flaring, whereas our data has a *softer* index in the flaring state.

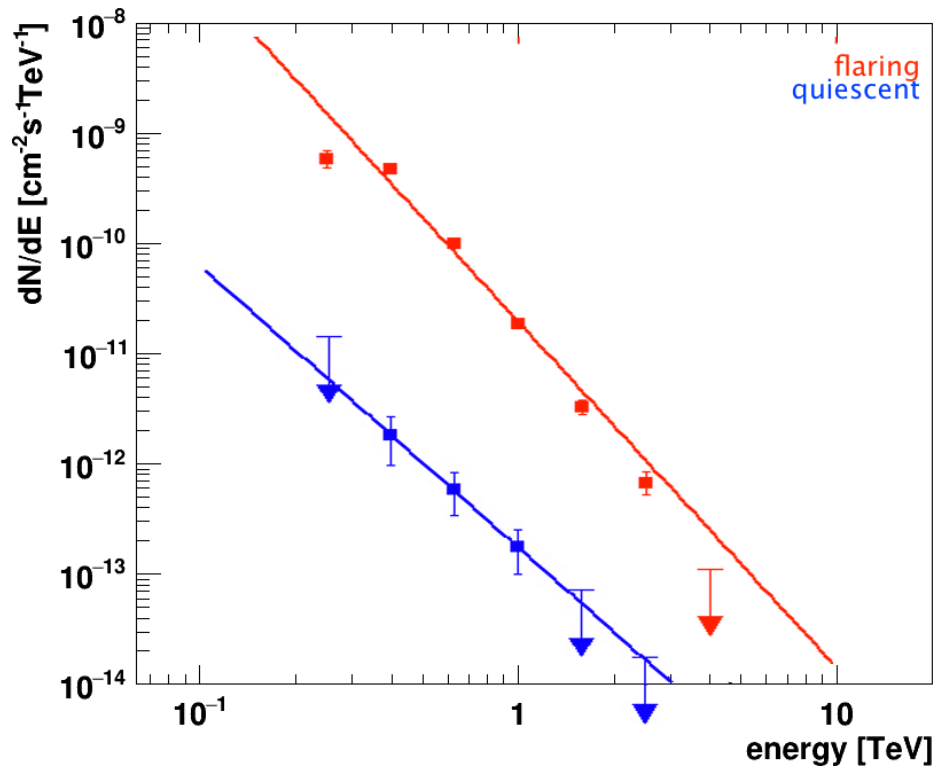


Figure 3.19: Comparison of the BL Lac energy spectrum in the flaring state and in the quiescent state. In red, the flaring spectrum. In blue, the quiescent spectrum. Arrows indicate 99%-confidence upper limits.

Chapter 4

BL Lacertae as seen by Fermi-LAT and Swift-XRT

To get a fuller picture of BL Lac's spectral behavior in the quiescent state versus in the flaring state, we now take our attention to two other wavelength intervals: [100 MeV-100 GeV] with the Fermi Gamma-Ray Space Telescope, and [0.3 - 10 keV] with the Swift X-Ray Telescope.

4.1 *Fermi-LAT*

The Fermi Gamma-Ray Space Telescope is a satellite-based observatory that was launched in 2008 (Figure 4.1). It hosts the Large Array Telescope, *Fermi-LAT*, which consists of 16 tracker modules, 16 calorimeter modules, and a segmented anti-coincidence detector. The tracker modules convert incident gamma-rays into an electron-positron pair whose energy is deposited in the calorimeter, thus measuring the photon's original direction and energy. *Fermi-LAT* detects gamma-rays in the 20 MeV-300GeV energy range. The 5-year all-sky gamma-ray map is seen in Figure 4.2. The bright diffuse emission at the centre corresponds to the galactic disk. As of its fourth catalogue, *Fermi-LAT* reports 5064 sources

of gamma-rays, and as seen in Figure 4.3, at high galactic latitudes, the vast majority of these are AGNs [Ajello et al., 2020].

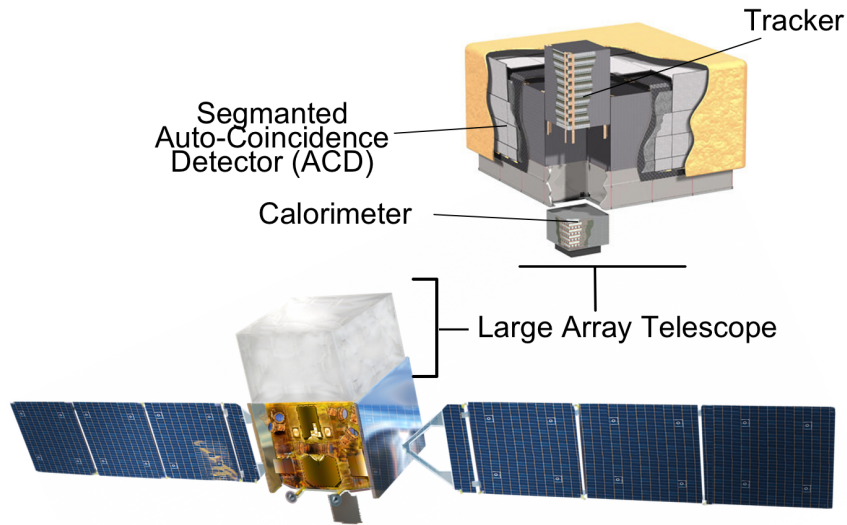


Figure 4.1: Artist's rendition of the Fermi Gamma-Ray Space Telescope. Adapted from Atwood et al. [2009]. The Large Array Telescope's dimensions are $1.8 \text{ m} \times 1.8 \text{ m} \times 0.72 \text{ m}$.

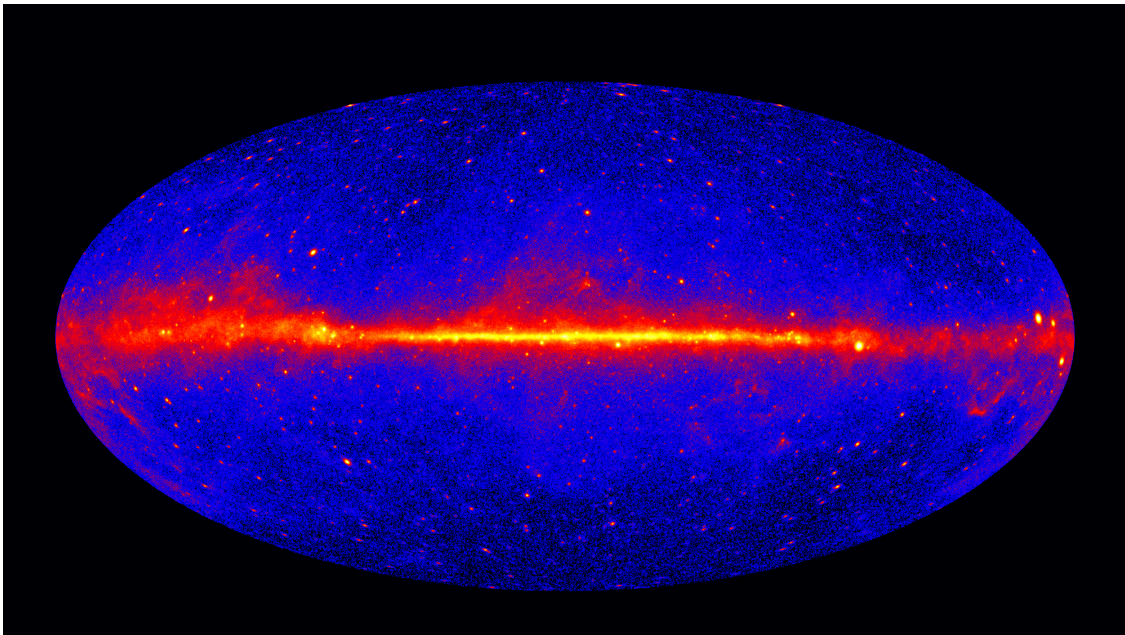


Figure 4.2: The *Fermi*-LAT five-year all-sky map. Energy range: [1-300 GeV] Image credit: NASA/DOE/*Fermi* LAT Collaboration.

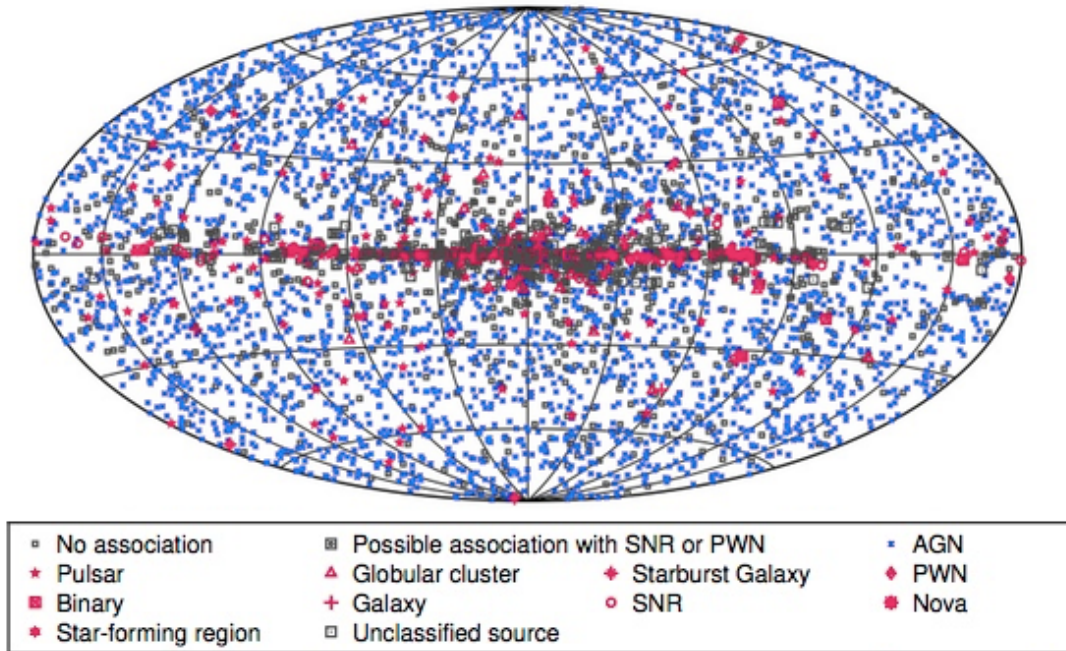


Figure 4.3: All sky map of *Fermi*-LAT sources as reported in their eight-year catalogue [Ajello et al., 2020]. Blue dots mark AGNs.

Fermi-LAT data and the tools to analyse it are open for public access and use, which made possible the analysis of BL Lac *Fermi*-LAT data presented in this section.

4.1.1 Data Selection

First, we retrieved the publicly available BL Lac light-curve¹ (Figure 4.4), which comprised 4346 days of data (*Fermi*-LAT sweeps out across most of the sky multiple times per day, so unlike the VERITAS data set, this data was taken daily). We performed the same Bayesian Block analysis as described in Section 3.1.3, and the data was sliced into 144 bins. The source displayed a lot of variability even when it was at a low flux, so the distinction between flaring and quiescent was not as obvious as with the VERITAS data (seen in Figure 3.17). After singling out the bins when the flux was more than twice the overall average, 37 flaring bins were identified (see Figure 4.5).

¹https://fermi.gsfc.nasa.gov/ssc/data/access/lat/msl_lc/source/BL_Lac

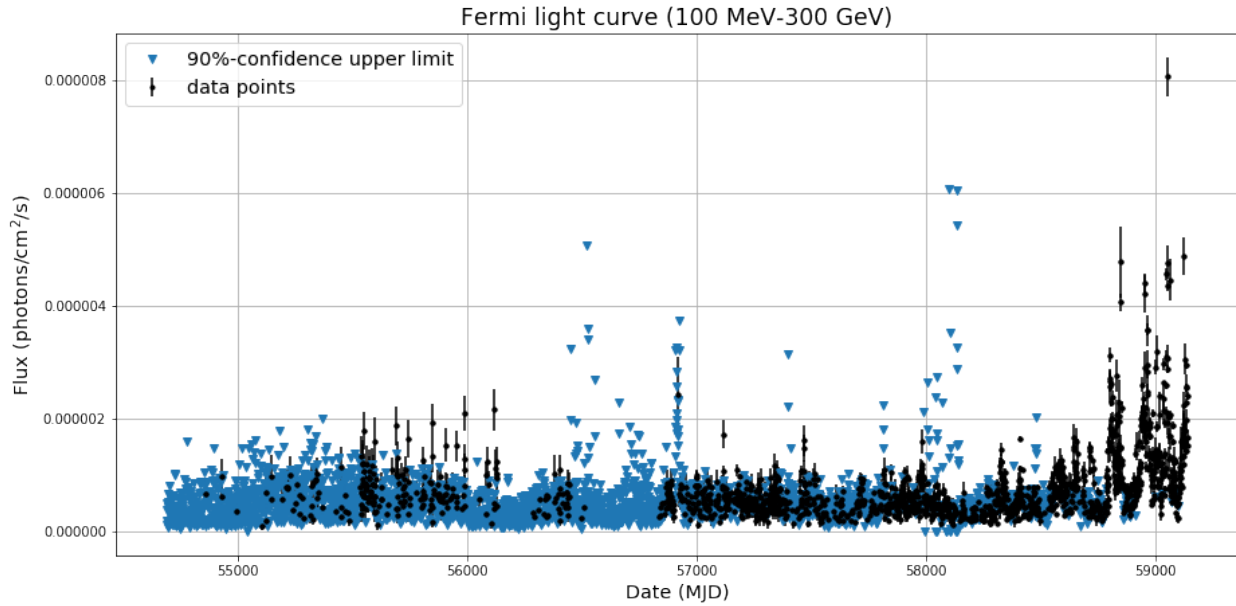


Figure 4.4: *Fermi*-LAT Lightcurve of BL Lac. Energy range: [100 MeV-300 GeV]

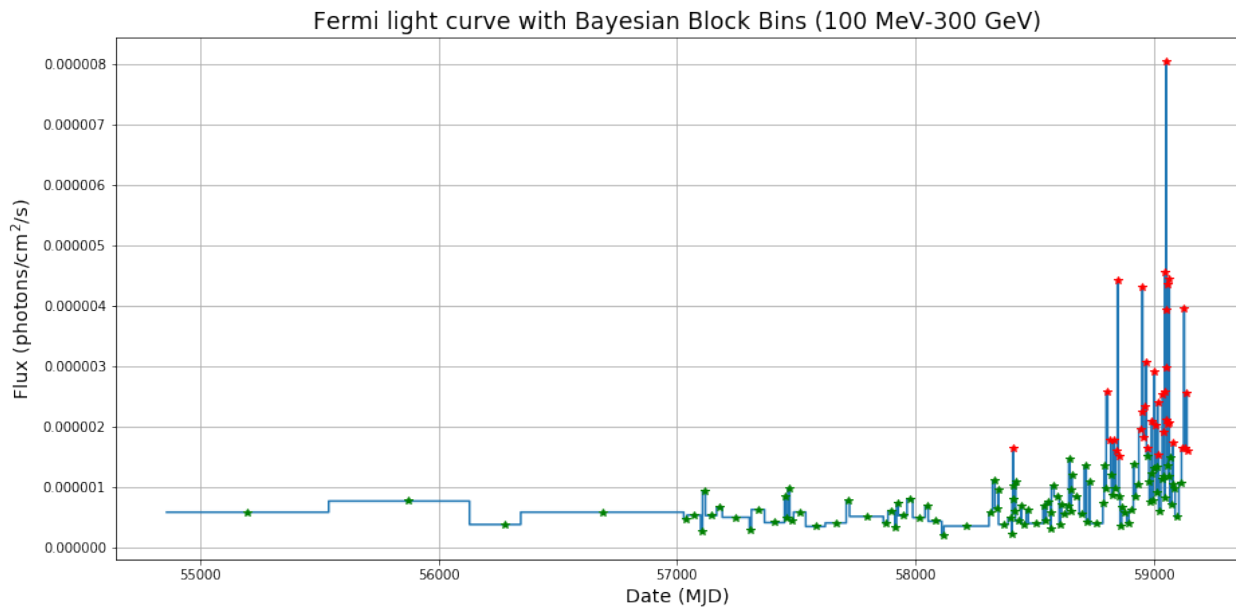


Figure 4.5: *Fermi*-LAT Lightcurve of BL Lac with Bayesian Block bins. Green stars mark bins where the average flux was less than twice the overall average flux. Red stars mark bins where the average flux was more than twice the overall average. Energy range: [100 MeV-300 GeV]

For the quiescent data set, a little over a year of data was selected from 56930 to 57390 (MJD).

4.1.2 Quiescent State Analysis

The data was then analysed using *Fermitools*² [Fermi Science Support Development Team, 2019]. In order to obtain the detection, flux determination and spectral modeling of BL Lac in the quiescent state, we performed a maximum likelihood optimization technique, described briefly here:

1. Download data from the *Fermi*-LAT archive. Here, over a year of data was selected, with a radius of 5° around BL Lacertae's coordinates, and we selected the energy range to be [100 MeV - 300 GeV]. We obtain event data files, and a spacecraft data file with information about the pointing and livetime history of the instrument.
2. Make count maps. This step takes the event files and displays photon arrival direction to create a skymap. The result of this step is seen in Figure 4.6, where BL lac is clearly detected in Fermi's energy range.
3. Create a source model file. This file contains the detected sources, their model parameters, such as the flux and spectral index, and the background models, which will be fit to the data. In this analysis, our region of interest contained 84 point-sources, though only two (BL Lac and FGL J2207.1+4316) were significant enough (over 3σ) to be included in our model (see Figure 4.7).
4. Make an exposure map. This step analyzes diffuse sources and derives absolute fluxes from photon counts.
5. Perform the maximum likelihood analysis. The data is fitted to the model, calculating flux, errors, spectral indices, and more. This gives a spectral model for the whole region.

²<https://fermi.gsfc.nasa.gov/ssc/data/analysis/>

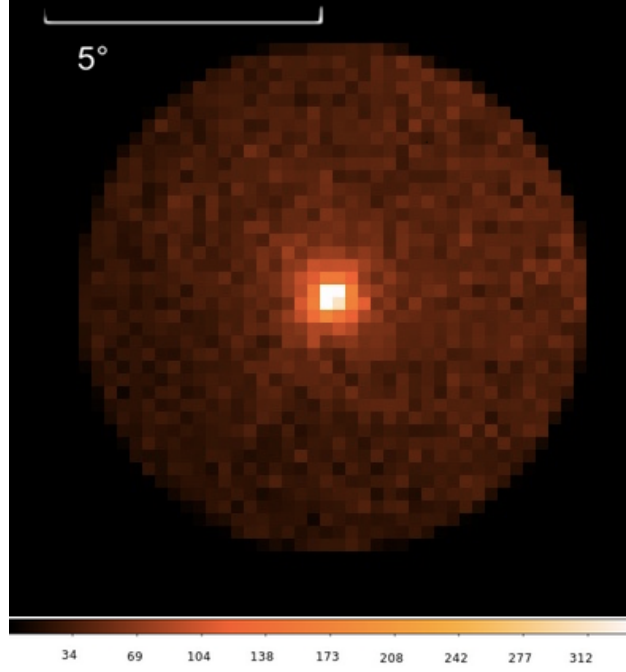


Figure 4.6: Count map of BL Lac in the quiescent state as seen by *Fermi*-LAT. The color-scale corresponds to the number of counted events per pixel.

6. Extract spectral information about BL Lac. Now that the whole region has been adequately modelled, the component due to BL Lac can be singled out and studied.

The result of this analysis is the spectrum seen in Figure 4.8, with the residual ([counts-model]/model). The best fit was found to be a log parabola:

$$\frac{dN}{dE} = N_0 \left(\frac{E}{E_b} \right)^{-(\alpha + \beta \log(E/E_b))} \quad (4.1)$$

Where E_b is a scale parameter that is usually kept fixed. Here, it was assigned a default value of 726.6 MeV. The best fit gave the following parameters:

$$\begin{aligned} N_{0Q} &= (10.8 \pm 0.2) \times 10^{-11} \text{ MeV}^{-1} \text{ s}^{-1} \text{ cm}^{-2} \\ \alpha_Q &= 1.76 \pm 0.02 \\ \beta_Q &= 0.21 \pm 0.01 \end{aligned} \quad (4.2)$$

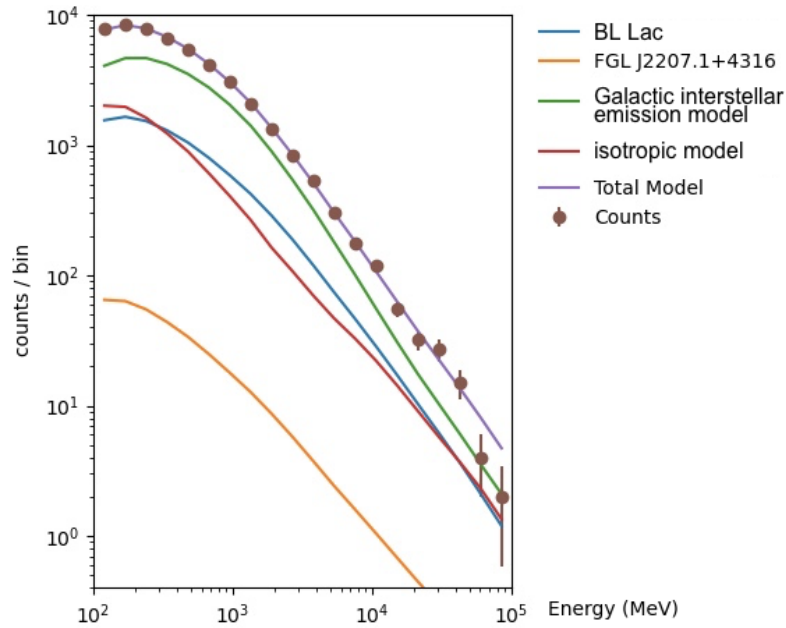


Figure 4.7: Best fit spectra of BL Lac and background sources. The galactic emission and isotropic models were built by the Fermi collaboration from the first 8 years of LAT data (Pass 8 P8 R3) [Acero et al., 2016]

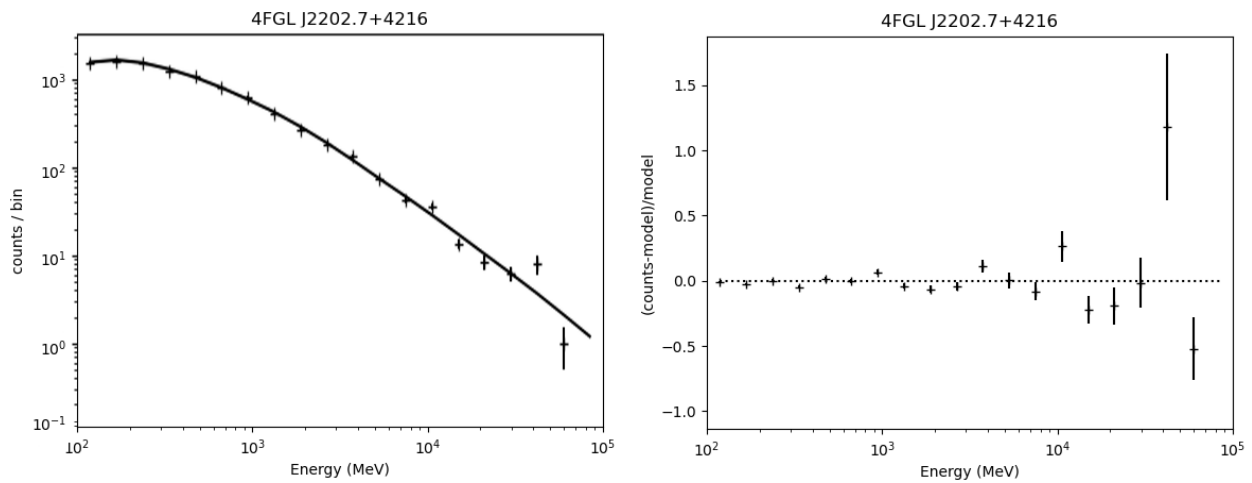


Figure 4.8: Left: Best fit spectrum of BL Lac in the quiescent state as seen by *Fermi*-LAT. Right: Model/Data residuals of the log-parabola fit of BL Lac in the quiescent state as seen by *Fermi*-LAT. This shows that the fit is very good up until the 10^4 MeV energy range, with some deviations at higher energies. (4FGL J2202.7+4216 is the name of BL Lac in the fourth Fermi Catalogue [Ajello et al., 2020].)

Finally, we want to compare this spectral information to BL Lac in the flaring state. For this we selected the date of October 6 2020 (MJD 59128), when the source displayed a record flare (see Figure 4.4). This was also best fit by a log parabola, with the following parameters:

$$\begin{aligned}
 N_{0F} &= (1.00 \pm 0.01) \times 10^{-9} \text{ MeV}^{-1} \text{ s}^{-1} \text{ cm}^{-2} \\
 \alpha_F &= 2.0 \pm 0.2 \\
 \beta_F &= 0.15 \pm 0.1
 \end{aligned}
 \tag{4.3}$$

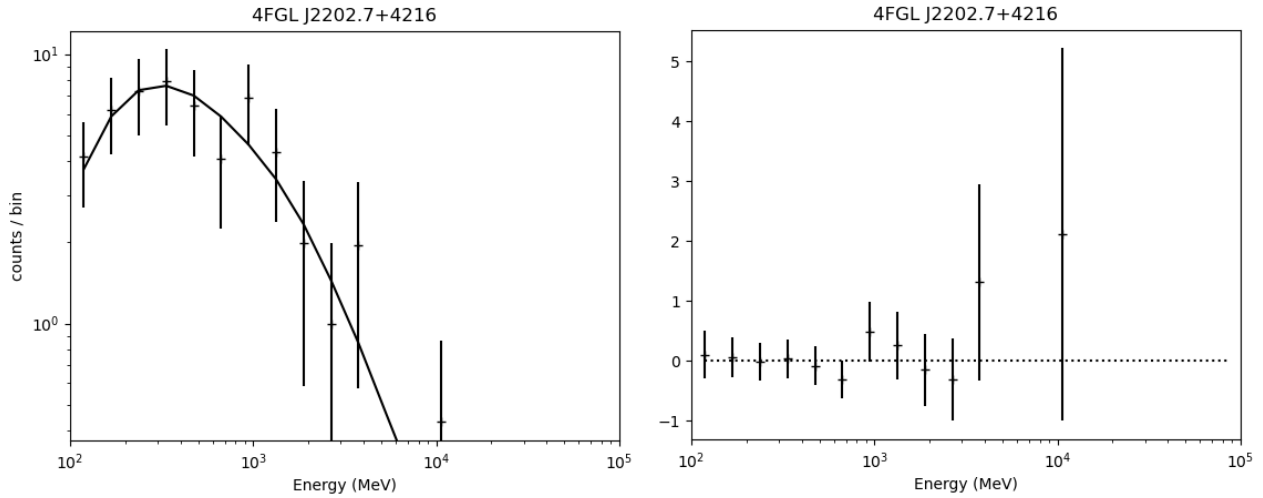


Figure 4.9: Left: Best fit spectrum of BL Lac in the flaring state as seen by *Fermi*-LAT. Right: Model/Data residuals of the log-parabola fit of BL Lac in the flaring state as seen by *Fermi*-LAT. 4FGL J2202.7+4216 is the name of BL Lac in the fourth Fermi Catalogue [Ajello et al., 2020]. This shows that the fit is fairly good up until the 10^3 MeV energy range, with a single deviation at 10^4 MeV. The spectrum cuts off above 10^4 MeV. (The counts are background subtracted, which is why the 10^4 MeV bin has gone under 1.)

We once again notice that the flaring state has different spectral parameters than the quiescent state. The two best-fit model fluxes are plotted in Figure 4.10. Most of the flaring photons are at energies below 10^4 MeV (see Figure 4.9), suggesting a strong cut-off in the emission process of the flaring component. Although thorough theoretical modelling is

outside the scope of this thesis, this could be due to more efficient cooling, such as, for instance, if the flaring component is located in a region of the jet with a stronger magnetic field.

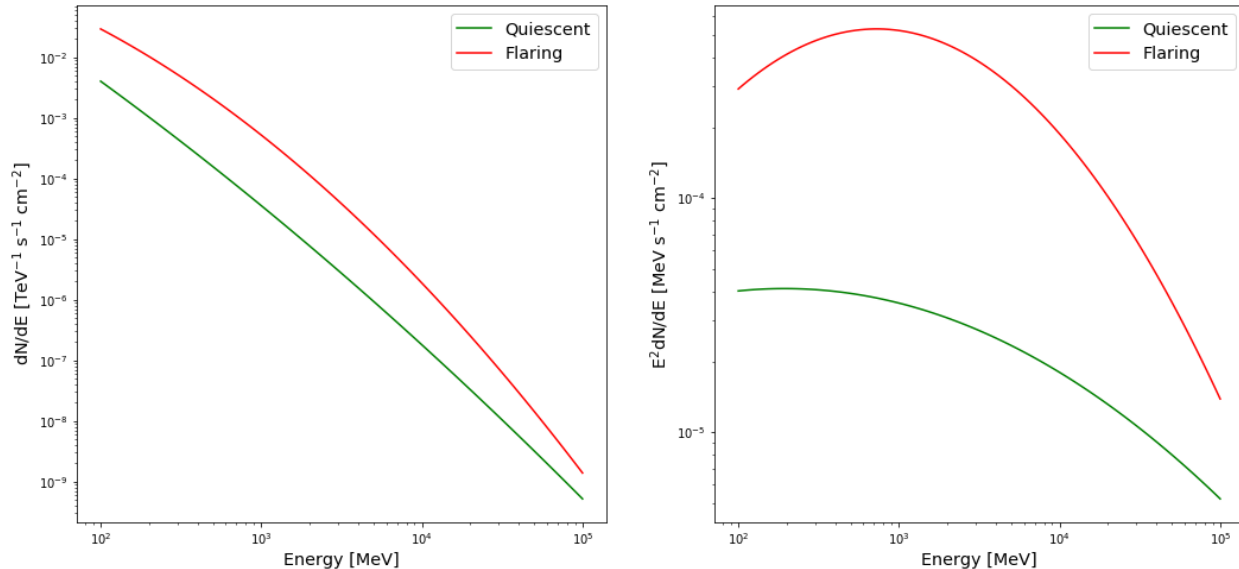


Figure 4.10: Plot of the best-fit model of BL Lac as seen by *Fermi*-LAT. The green line is for the quiescent state, the red line is for the October 6 2020 flare. On the left is the dN/dE spectrum, on the right is the $E^2 dN/dE$.

4.2 Swift-XRT

The Neil Gehrels Swift observatory (Swift) [Gehrels et al., 2004] is a multi-wavelength, rapid response satellite observatory launched in 2004 by NASA (Figure 4.11). One of the three instruments carried by the telescope is a narrow-field X-ray telescope (XRT) [Burrows et al., 2005], which detects photons in the energy range 0.2-10 keV. Originally designed to detect gamma-ray bursts (GRBs) and their afterglow, Swift-XRT expanded beyond that original goal by detecting around 36000 non-GRB, distinct, point-like sources in its first 7 years of observations [D’Elia et al., 2013]. Due to its flexible observing strategy and fast response to potential alerts to observe a target, Swift is ideal for multi-wavelength

observations, and it has also been monitoring 176 gamma-ray sources, most of which are blazars [Stroh and Falcone, 2013]. BL Lac is one of those sources.

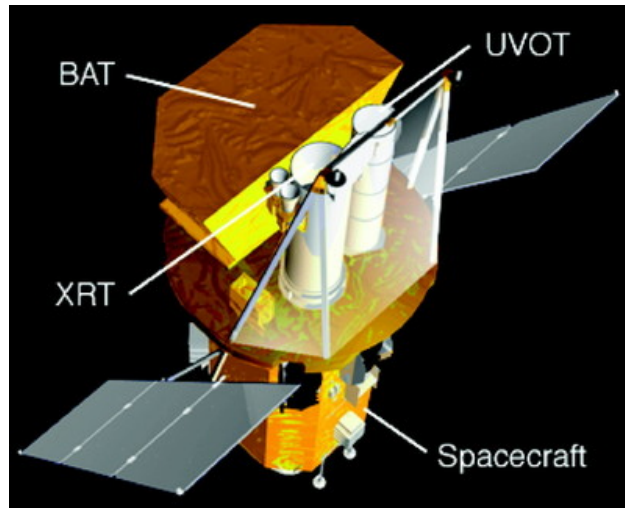


Figure 4.11: Artist's rendition of the Neil Gehrels Swift Observatory. XRT: X-ray telescope. BAT: burst alert telescope. UVOT: UV/optical telescope. From [Gehrels et al., 2004]

4.2.1 Data Selection

For the purpose of this analysis, we first retrieved the publicly available Swift light-curve³ (Figure 4.12). The data spanned from July 2005 to February 2021, and comprised 626 days.

Then, we applied the Bayesian Block method described in section 3.1.3 (Figure 4.13). The source displayed a lot of variability even when it was at a low flux, so the distinction between flaring and quiescent was not as obvious as with the VERITAS data (seen in Figure 3.17). After singling out the dates when the flux was more than twice the overall average, five main flaring blocks were identified (as seen in Figure 4.13):

- An extended medium flaring period from 56237 to 56308 (MJD).

³<https://www.swift.psu.edu/monitoring/source.php?source=BLLacertae>

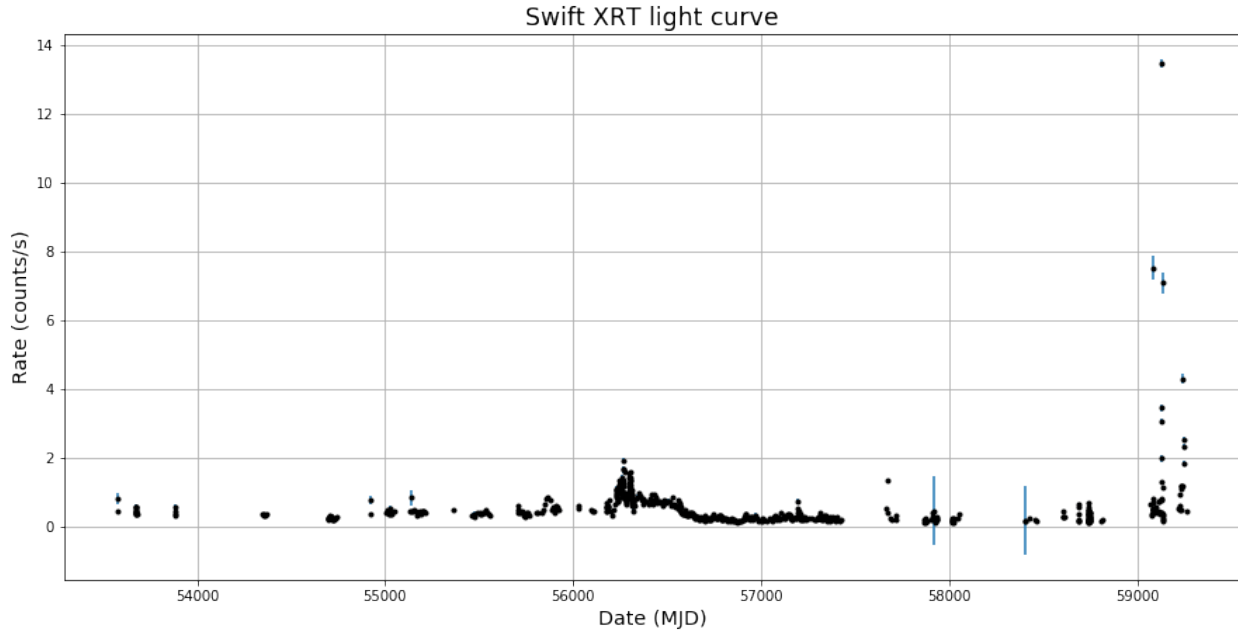


Figure 4.12: Swift-XRT light-curve of BL Lacertae.

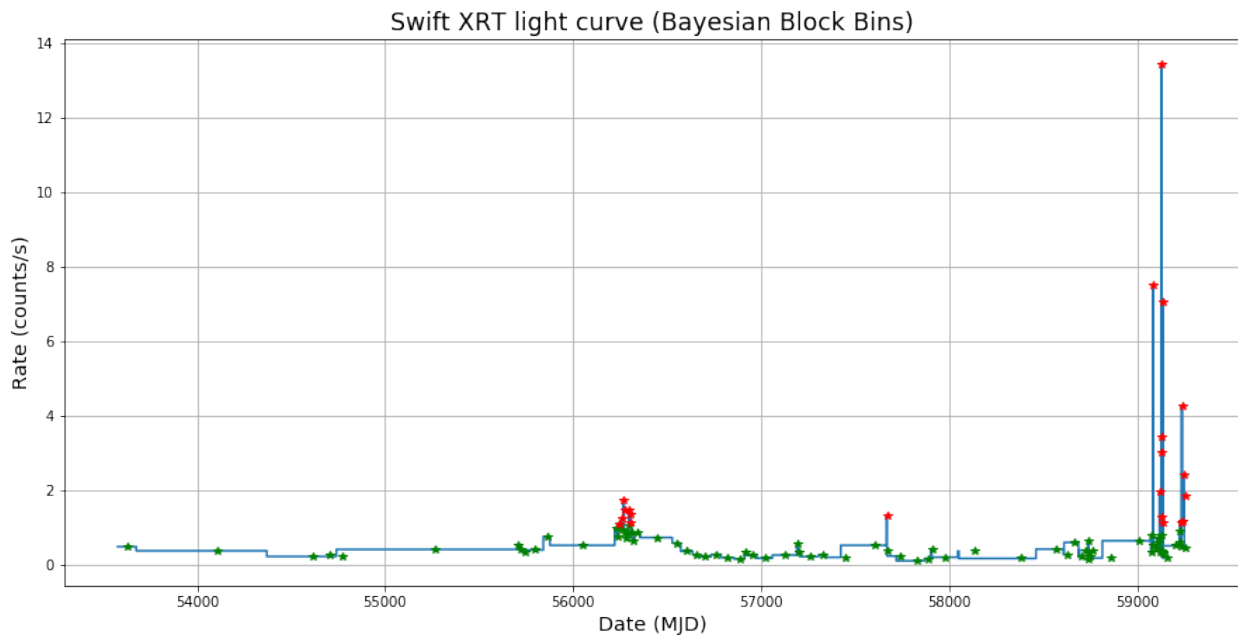


Figure 4.13: Swift-XRT light-curve of BL Lacertae with Bayesian Block bins. Green stars mark bins where the average flux was less than twice the overall average flux. Red stars mark bins where the average flux was more than twice the overall average.

- On 57667, a medium flare. (This is an interesting one as it nearly coincides with the flare measured by VERITAS on 57666, and it is the only flare that displays a correlation between VHE and X-ray energies.)
- On 59083, a bright flare.
- An extended bright flaring period from 59121 to 59135.
- An extended bright flaring period from 59229 to 59255.

All these dates and their close neighbours were excluded to construct the quiescent data set, which comprised 498 days, amounting to around 160 hours on source.

4.2.2 Quiescent State Analysis

Next, the Swift-XRT online analyser [Evans et al., 2009] was used.⁴ This software can produce five types of data products: images, light curves, enhanced positions, source detection, and spectra.

Figure 4.14 shows the resulting sky map of BL Lac in the quiescent state. At the location of the source, 148107 events were counted, and 2547 background, resulting in a count rate of $0.3323 \pm 0.0009s^{-1}$. Information about the Swift-XRT method for source detection can be found in Evans et al. [2020].

⁴<https://www.swift.ac.uk/user.objects>

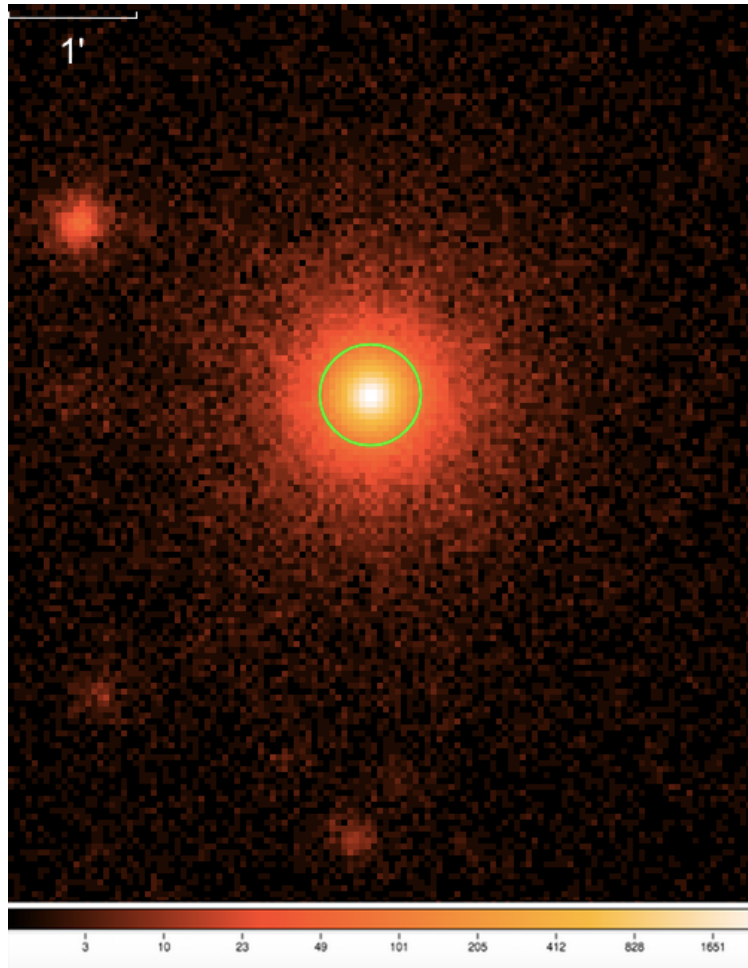


Figure 4.14: Sky map of BL Lac in the quiescent state as seen by Swift-XRT. The green circle is centred on the coordinates of BL Lac. At that source location, 148107 events were counted, and 2547 background, resulting in a count rate of $0.3323 \pm 0.0009 s^{-1}$. The position error is of $5.0''$. Energy range is [0.3-10 keV].

The method of spectral reconstruction is described in Evans et al. [2009]. The time-averaged spectra can be seen in Figure 4.15. The two colors, labelled as WT and PC, correspond to two of the four Swift-XRT operating modes: respectively, Windowed Timing (WT) mode, and Photon Counting (PC) mode. In WT mode, images are one-dimensional strips of data oriented at the space craft roll angle, with a time resolution of 1.8ms. In PC mode, images are two-dimensional, with a 2.5 second time resolution. (For more detail on these two modes, see Gehrels et al. [2004].) PC mode is best used for low-flux sources

(< 1 mCrab), whereas WT mode is best for sources with fluxes between 1 and 600 mCrab [Burrows et al., 2005]. This means that when measuring the flux in the quiescent state, where the flux is low, we only need to take into account the PC mode.

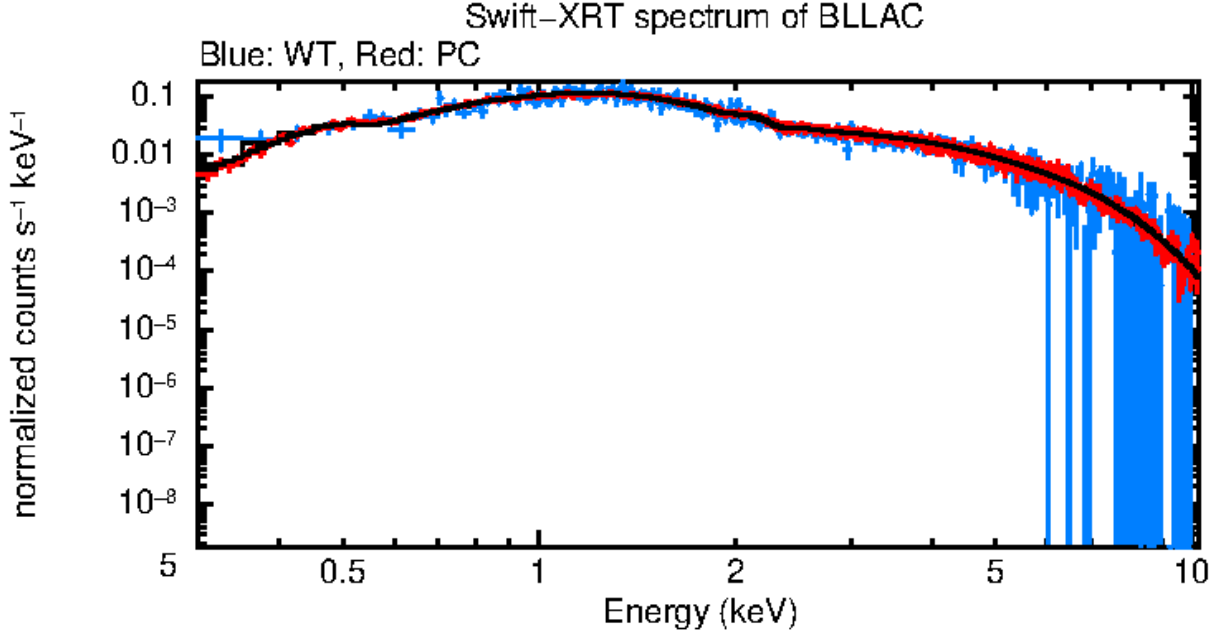


Figure 4.15: Quiescent spectra of BL Lac as seen by Swift-XRT. Blue: Windowed Timing mode. Red: Photon Counting mode. Black: absorbed-power law model.

Using the Swift analysis package, the obtained spectrum is automatically fitted with absorbed power-law models that takes into account galactic absorption (using data from the Leiden/Argentine/Bonn (LAB) Survey of Galactic HI [Kalberla et al., 2005]). In the quiescent state, the time-average spectrum of BL Lac is best fit by a gas column density of $N_H = (2.87 \pm 0.06) \times 10^{21} \text{cm}^{-2}$, and a photon index of:

$$\Gamma_Q = 1.72 \pm 0.01 \tag{4.4}$$

Where Γ_Q is the index of the power law:

$$\frac{dF}{dE} = F_0 \left(\frac{E}{E_0} \right)^{-\Gamma} \tag{4.5}$$

For comparison, a flaring data set was also selected. The event list comprised 11 days, from 59124 to 59135 (the fourth flaring period previously mentioned).

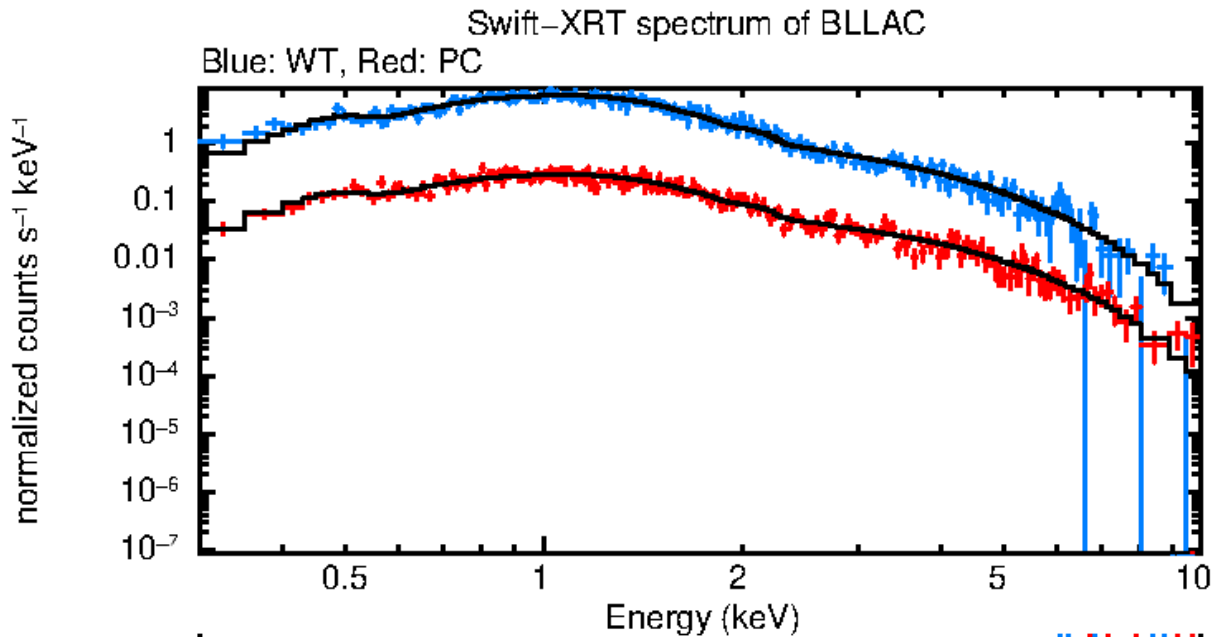


Figure 4.16: Flaring spectra of BL Lac as seen by Swift-XRT. Blue: Windowed Timing mode. Red: Photon Counting mode. Black: absorbed-power law model.

Figure 4.16 shows the time-averaged flaring spectrum. For the fit, the gas density column N_H was found to be the same within errors (as expected) but the flaring spectral index was very different:

$$\Gamma_Q = 2.34 \pm 0.06 \quad (4.6)$$

Figure 4.17 shows a plot of the best fit for each spectrum. Here, our fit points clearly to the spectral index being softer when the source is flaring. Similarly to the VHE data, this is different from the typical "harder when brighter" behavior of HBL blazars. A possible interpretation of this result can be found with a multi emission zone model [Abeysekara et al., 2018]. A large component (photon index < 2) emitting via inverse Compton could dominate in the quiescent state, while during flares, a compact component (photon index > 2) emitting via synchrotron would dominate.

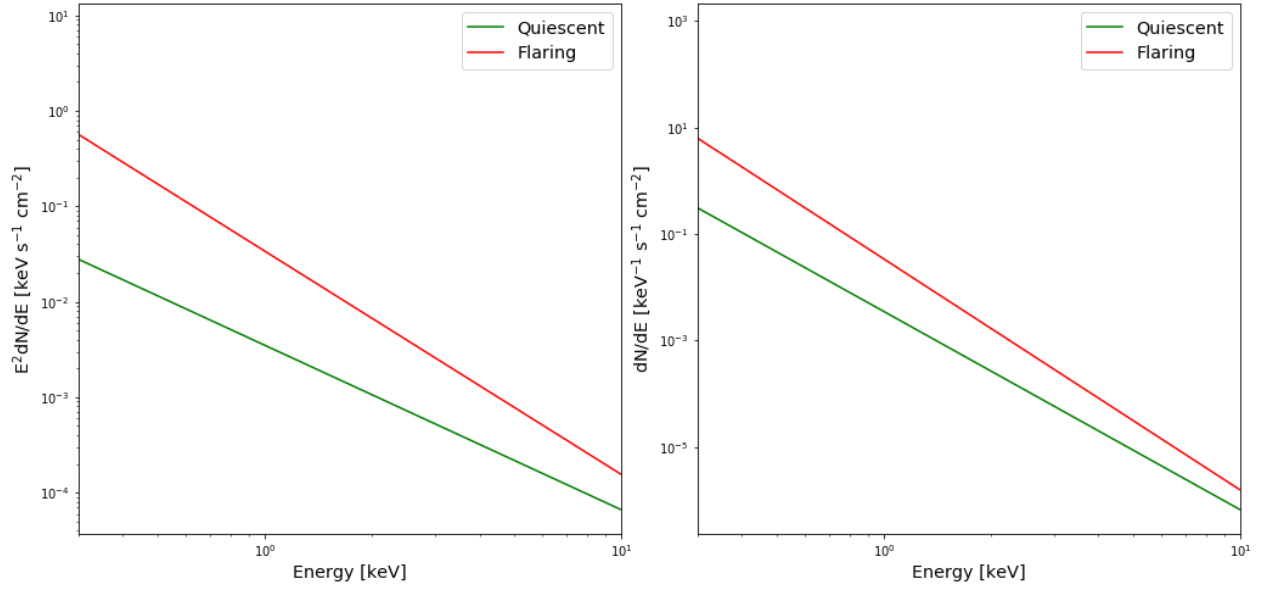


Figure 4.17: Plot of the best-fit model of BL Lac as seen by Swift-XRT. Green is for the quiescent data set, red is for the flaring data set. On the left is the $E^2 dN/dE$ spectrum. On the right is the dN/dE spectrum.

Chapter 5

Conclusions

This thesis has looked at BL Lac in the quiescent state and compared it to its flaring state using gamma-ray and X-ray data. After using a Bayesian Block method to determine when the source was flaring, we analysed 11 years of archival VERITAS data and found a weak detection of BL Lac in the quiescent state (4.3σ). The spectra were fit with a power-law model, and we found that the spectral index of BL Lac appears to be harder or equal when the source is quiescent, which would be an unusual behavior for HBLs. We also cannot fully exclude that the quiescent emission is contaminated by another VHE source, such as a supernova remnant.

We also looked at BL Lac data at other energies: first in the lower energy gamma-rays (100 MeV-300 GeV) with *Fermi*-LAT, then in the X-ray (0.3-10keV) with Swift-XRT. At lower gamma-ray energies, the spectra were best fit by a log parabola, and the quiescent state showed different spectral parameters from the flaring state. In the flaring state, we observe that most photons were at lower energies, which could suggest a strong a cut-off in the emission process of the flaring component. At X-ray energies, the spectra were best fit by an absorbed power law, and the spectral index was much harder when BL Lac was quiescent. This X-ray emission could be explained by a multi emission zone model, with

a larger component emitting via inverse Compton dominating in the quiescent state, and a more compact component emitting via synchrotron dominating during flares.

In the future, this analysis could be pushed further by looking at observations of BL Lac at other wavelengths, such as UV, optical, infrared, and radio, which could be combined to form the full SED and study the double-hump structure. Another interesting avenue to explore would be to study the quiescent states of other BL Lac objects (such as, for instance, Markarian 421) to look for any similarities and differences. An in-depth comparison to existing theoretical blazar models would be valuable. Finally, future generations of IACTs (such as the Cherenkov Telescope Array) will surely observe BL Lacertae with even better sensitivity, and provide more information about the source's quiescent state.

Bibliography

M. Aartsen, M. Ackermann, J. Adams, J. Aguilar, M. Ahlers, M. Ahrens, D. Altmann, K. Andeen, T. Anderson, I. Anseau, and et al. The icecube neutrino observatory: instrumentation and online systems. *Journal of Instrumentation*, 12(03):P03012–P03012, Mar 2017. ISSN 1748-0221. doi: 10.1088/1748-0221/12/03/p03012. URL <http://dx.doi.org/10.1088/1748-0221/12/03/P03012>.

A. U. Abeysekara, W. Benbow, R. Bird, T. Brantseg, R. Brose, M. Buchovecky, J. H. Buckley, V. Bugaev, M. P. Connolly, W. Cui, M. K. Daniel, A. Falcone, Q. Feng, J. P. Finley, L. Fortson, A. Furniss, G. H. Gillanders, I. Gunawardhana, M. Hütten, D. Hanna, O. Hervet, J. Holder, G. Hughes, T. B. Humensky, C. A. Johnson, P. Kaaret, P. Kar, M. Kertzman, F. Krennrich, M. J. Lang, T. T. Y. Lin, S. McArthur, P. Moriarty, R. Mukherjee, S. O'Brien, R. A. Ong, A. N. Otte, N. Park, A. Petrashyk, M. Pohl, E. Pueschel, J. Quinn, K. Ragan, P. T. Reynolds, G. T. Richards, E. Roache, C. Rulten, I. Sadeh, M. Santander, G. H. Sembroski, K. Shahinyan, S. P. Wakely, A. Weinstein, R. M. Wells, P. Wilcox, D. A. Williams, B. Zitzer, S. G. Jorstad, A. P. Marscher, M. L. Lister, Y. Y. Kovalev, A. B. Pushkarev, T. Savolainen, I. Agudo, S. N. Molina, J. L. Gómez, V. M. Larionov, G. A. Borman, A. A. Mokrushina, M. Tornikoski, A. Lähteenmäki, W. Chamani, S. Enestam, S. Kiehlmann, T. Hovatta, P. S. Smith, and P. P. and. Multiwavelength observations of the blazar BL lacertae: A new fast TeV gamma-ray flare. *The Astrophysical Journal*, 856(2):95, mar 2018. doi: 10.3847/1538-4357/aab35c. URL <https://doi.org/10.3847/1538-4357/aab35c>.

- F. Acero, M. Ackermann, M. Ajello, A. Albert, L. Baldini, J. Ballet, G. Barbiellini, D. Bastieri, R. Bellazzini, E. Bissaldi, and et al. Development of the model of galactic interstellar emission for standard point-source analysis of fermi large area telescope data. *The Astrophysical Journal Supplement Series*, 223(2):26, Apr 2016. ISSN 1538-4365. doi: 10.3847/0067-0049/223/2/26. URL <http://dx.doi.org/10.3847/0067-0049/223/2/26>.
- F. Aharonian, L. Bergstroem, and C. Dermer. *Astrophysics at Very High Energies*. Springer; Berlin (Germany), 2013.
- M. Ajello, R. Angioni, M. Axelsson, J. Ballet, G. Barbiellini, D. Bastieri, J. Becerra Gonzalez, R. Bellazzini, E. Bissaldi, E. D. Bloom, and et al. The fourth catalog of active galactic nuclei detected by the fermi large area telescope. *The Astrophysical Journal*, 892(2):105, Apr 2020. ISSN 1538-4357. doi: 10.3847/1538-4357/ab791e. URL <http://dx.doi.org/10.3847/1538-4357/ab791e>.
- D. M. Alexander and R. C. Hickox. What drives the growth of black holes? , 56(4):93–121, June 2012. doi: 10.1016/j.newar.2011.11.003.
- Astropy Collaboration, A. M. Price-Whelan, B. M. Sipőcz, H. M. Günther, P. L. Lim, S. M. Crawford, S. Conseil, D. L. Shupe, M. W. Craig, N. Dencheva, A. Ginsburg, J. T. VanderPlas, L. D. Bradley, D. Pérez-Suárez, M. de Val-Borro, T. L. Aldcroft, K. L. Cruz, T. P. Robitaille, E. J. Tollerud, C. Ardelean, T. Babej, Y. P. Bach, M. Bachetti, A. V. Bakanov, S. P. Bamford, G. Barentsen, P. Barmby, A. Baumbach, K. L. Berry, F. Biscani, M. Bouchier, K. A. Bostroem, L. G. Bouma, G. B. Brammer, E. M. Bray, H. Breytenbach, H. Buddelmeijer, D. J. Burke, G. Calderone, J. L. Cano Rodríguez, M. Cara, J. V. M. Cardoso, S. Cheedella, Y. Copin, L. Corrales, D. Crichton, D. D’Avella, C. Deil, É. Depagne, J. P. Dietrich, A. Donath, M. Droettboom, N. Earl, T. Erben, S. Fabbro, L. A. Ferreira, T. Finethy, R. T. Fox, L. H. Garrison, S. L. J. Gibbons, D. A. Goldstein, R. Gommers, J. P. Greco, P. Greenfield, A. M. Groener, F. Grollier, A. Hagen, P. Hirst, D. Homeier, A. J. Horton, G. Hosseinzadeh, L. Hu, J. S. Hunkeler, Ž. Ivezić, A. Jain, T. Jenness,

G. Kanarek, S. Kendrew, N. S. Kern, W. E. Kerzendorf, A. Khvalko, J. King, D. Kirkby, A. M. Kulkarni, A. Kumar, A. Lee, D. Lenz, S. P. Littlefair, Z. Ma, D. M. Macleod, M. Mastropietro, C. McCully, S. Montagnac, B. M. Morris, M. Mueller, S. J. Mumford, D. Muna, N. A. Murphy, S. Nelson, G. H. Nguyen, J. P. Ninan, M. Nöthe, S. Ogaz, S. Oh, J. K. Parejko, N. Parley, S. Pascual, R. Patil, A. A. Patil, A. L. Plunkett, J. X. Prochaska, T. Rastogi, V. Reddy Janga, J. Sabater, P. Sakurikar, M. Seifert, L. E. Sherbert, H. Sherwood-Taylor, A. Y. Shih, J. Sick, M. T. Silbiger, S. Singanamalla, L. P. Singer, P. H. Sladen, K. A. Sooley, S. Sornarajah, O. Streicher, P. Teuben, S. W. Thomas, G. R. Tremblay, J. E. H. Turner, V. Terrón, M. H. van Kerkwijk, A. de la Vega, L. L. Watkins, B. A. Weaver, J. B. Whitmore, J. Woillez, V. Zabalza, and Astropy Contributors. The Astropy Project: Building an Open-science Project and Status of the v2.0 Core Package. *Astronomical Journal*, 156(3):123, Sept. 2018. doi: 10.3847/1538-3881/aabc4f.

W. B. Atwood, A. A. Abdo, M. Ackermann, W. Althouse, B. Anderson, M. Axelsson, L. Baldini, J. Ballet, D. L. Band, G. Barbiellini, and et al. The large area telescope on thefermi gamma-ray space telescopemission. *The Astrophysical Journal*, 697(2): 1071–1102, May 2009. ISSN 1538-4357. doi: 10.1088/0004-637x/697/2/1071. URL <http://dx.doi.org/10.1088/0004-637x/697/2/1071>.

M. Boettcher. Progress in multiwavelength and multi-messenger observations of blazars and theoretical challenges. *Galaxies*, Special Issue "Cosmic Plasmas and Electromagnetic Phenomena", 2019.

R. Brun and F. Rademakers. Root - an object oriented data analysis framework. In *AIHENP'96 Workshop, Lausanne*, volume 389, pages 81–86, 1996.

D. N. Burrows, J. E. Hill, J. A. Nousek, J. A. Kennea, A. Wells, J. P. Osborne, A. F. Abbey, A. Beardmore, K. Mukerjee, A. D. T. Short, G. Chincarini, S. Campana, O. Citterio, A. Moretti, C. Pagani, G. Tagliaferri, P. Giommi, M. Capalbi, F. Tamburelli, L. Angelini, G. Cusumano, H. W. Bräuninger, W. Burkert, and G. D. Hartner. The Swift

- X-Ray Telescope. *Space Science Reviews*, 120(3-4):165–195, Oct. 2005. doi: 10.1007/s11214-005-5097-2.
- S. Ciprini, M. Busso, and G. Tosti. The infrared peak of the blazar spectral energy distribution and the monitoring from antarctica. *Memorie della Societa Astronomica Italiana*, 74:70, 01 2003.
- P. Cogan. *Nanosecond Sampling of Atmospheric Cherenkov Radiation Applied to TeV Gamma-Ray Observations of Blazars with VERITAS*. PhD thesis, University College Dublin, 2006.
- G. Cowan. *Statistical data analysis*. Oxford University Press, USA, 1998.
- C. Davies. Design of the quartermaster solar furnace. *The Proceedings of the Solar Furnace Symposium.*, 2-3(1):16 – 22, 1957.
- V. D’Elia, M. Perri, S. Puccetti, M. Capalbi, P. Giommi, D. N. Burrows, S. Campana, G. Tagliaferri, G. Cusumano, P. Evans, N. Gehrels, J. Kennea, A. Moretti, J. A. Nousek, J. P. Osborne, P. Romano, and G. Stratta. The seven year Swift-XRT point source catalog (1SWXRT). *Astronomy and Astrophysics*, 551:A142, Mar. 2013. doi: 10.1051/0004-6361/201220863.
- P. A. Evans, A. P. Beardmore, K. L. Page, J. P. Osborne, P. T. O’Brien, R. Willingale, R. L. C. Starling, D. N. Burrows, O. Godet, L. Vetere, and et al. Methods and results of an automatic analysis of a complete sample of swift-xrt observations of grbs. *Monthly Notices of the Royal Astronomical Society*, 397(3):1177–1201, Aug 2009. ISSN 1365-2966. doi: 10.1111/j.1365-2966.2009.14913.x. URL <http://dx.doi.org/10.1111/j.1365-2966.2009.14913.x>.
- P. A. Evans, K. L. Page, J. P. Osborne, A. P. Beardmore, R. Willingale, D. N. Burrows, J. A. Kennea, M. Perri, M. Capalbi, G. Tagliaferri, and et al. 2sxs: An improved and expanded swift x-ray telescope point-source catalog. *The Astrophysical Journal Supplement Series*, 247(2):54, Apr 2020. ISSN 1538-4365. doi: 10.3847/1538-4365/ab7db9. URL <http://dx.doi.org/10.3847/1538-4365/ab7db9>.

D. J. Fegan. Gamma hadron separation at TeV energies. *Journal of Physics G: Nuclear and Particle Physics*, 23(9):1013–1060, sep 1997. doi: 10.1088/0954-3899/23/9/004. URL <https://doi.org/10.1088/0954-3899/23/9/004>.

Fermi Science Support Development Team. Fermitools: Fermi Science Tools, May 2019.

W. Galbraith and J. V. Jelley. Light pulses from the night sky associated with cosmic rays. *Nature*, 171(4347):349–350, 1953. doi: 10.1038/171349a0. URL <https://doi.org/10.1038/171349a0>.

S. Gammell. *A Search for Very High Energy Gamma-ray Emission from Active Galactic Nuclei using Multivariate Analysis*. PhD thesis, University College Dublin, 2004.

N. Gehrels, G. Chincarini, P. Giommi, K. O. Mason, J. A. Nousek, A. A. Wells, N. E. White, S. D. Barthelmy, D. N. Burrows, L. R. Cominsky, K. C. Hurley, F. E. Marshall, P. Mészáros, P. W. A. Roming, L. Angelini, L. M. Barbier, T. Belloni, S. Campana, P. A. Caraveo, M. M. Chester, O. Citterio, T. L. Cline, M. S. Cropper, J. R. Cummings, A. J. Dean, E. D. Feigelson, E. E. Fenimore, D. A. Frail, A. S. Fruchter, G. P. Garmire, K. Gendreau, G. Ghisellini, J. Greiner, J. E. Hill, S. D. Hunsberger, H. A. Krimm, S. R. Kulkarni, P. Kumar, F. Lebrun, N. M. Lloyd-Ronning, C. B. Markwardt, B. J. Mattson, R. F. Mushotzky, J. P. Norris, J. Osborne, B. Paczynski, D. M. Palmer, H. S. Park, A. M. Parsons, J. Paul, M. J. Rees, C. S. Reynolds, J. E. Rhoads, T. P. Sasseen, B. E. Schaefer, A. T. Short, A. P. Smale, I. A. Smith, L. Stella, G. Tagliaferri, T. Takahashi, M. Tashiro, L. K. Townsley, J. Tueller, M. J. L. Turner, M. Vietri, W. Voges, M. J. Ward, R. Willingale, F. M. Zerbi, and W. W. Zhang. The Swift Gamma-Ray Burst Mission. *Astrophysical Journal*, 611(2):1005–1020, Aug. 2004. doi: 10.1086/422091.

G. Ghisellini. *Synchrotron Self-Compton*, pages 89–93. Springer International Publishing, Heidelberg, 2013. ISBN 978-3-319-00612-3. doi: 10.1007/978-3-319-00612-3_6. URL https://doi.org/10.1007/978-3-319-00612-3_6.

- D. Heck, J. Knapp, J. N. Capdevielle, G. Schatz, and T. Thouw. CORSIKA: A Monte Carlo code to simulate extensive air showers. *report FZKA-6019*, 1998.
- A. M. Hillas. Cerenkov Light Images of EAS Produced by Primary Gamma Rays and by Nuclei. In *19th International Cosmic Ray Conference (ICRC19), Volume 3*, page 445, Aug. 1985.
- W. Hofmann, I. Jung, A. Konopelko, H. Krawczynski, H. Lampeitl, and G. Pühlhofer. Comparison of techniques to reconstruct vhe gamma-ray showers from multiple stereoscopic cherenkov images. *Astroparticle Physics*, 12(3):135–143, 1999. ISSN 0927-6505. doi: [https://doi.org/10.1016/S0927-6505\(99\)00084-5](https://doi.org/10.1016/S0927-6505(99)00084-5). URL <https://www.sciencedirect.com/science/article/pii/S0927650599000845>.
- J. Holder. Exploiting VERITAS Timing Information. In *29th International Cosmic Ray Conference (ICRC29), Volume 5*, page 383, Jan. 2005.
- IceCube Collaboration, Fermi-LAT, MAGIC, AGILE, ASAS-SN, HAWC, HESS, INTEGRAL, Kanata, Kiso, Kapteyn, Liverpool Telescope, Subaru, Swift/NuSTAR, VERITAS, and VLA/17B-403. Multimessenger observations of a flaring blazar coincident with high-energy neutrino icecube-170922a. *Science*, 361(6398), 2018. ISSN 0036-8075. doi: [10.1126/science.aat1378](https://doi.org/10.1126/science.aat1378). URL <https://science.sciencemag.org/content/361/6398/eaat1378>.
- P. M. W. Kalberla, W. B. Burton, D. Hartmann, E. M. Arnal, E. Bajaja, R. Morras, and W. G. L. Pöppel. The leiden/argentine/bonn (lab) survey of galactic hi. *Astronomy Astrophysics*, 440(2):775–782, Sep 2005. ISSN 1432-0746. doi: [10.1051/0004-6361:20041864](https://doi.org/10.1051/0004-6361:20041864). URL <http://dx.doi.org/10.1051/0004-6361:20041864>.
- K. Kotera and A. V. Olinto. The astrophysics of ultrahigh-energy cosmic rays. *Annual Review of Astronomy and Astrophysics*, 49(1):119–153, 2011. doi: [10.1146/annurev-astro-081710-102620](https://doi.org/10.1146/annurev-astro-081710-102620). URL <https://doi.org/10.1146/annurev-astro-081710-102620>.

- M. Krause. *High-sensitivity analysis of the Cygnus region observed with VERITAS*. PhD thesis, Humboldt U., Berlin (main), 2017.
- M. Krause, E. Pueschel, and G. Maier. Improved gamma hadron separation for the detection of faint γ -ray sources using boosted decision trees. *Astroparticle Physics*, 89:1–9, 2017. ISSN 0927-6505. doi: <https://doi.org/10.1016/j.astropartphys.2017.01.004>. URL <https://www.sciencedirect.com/science/article/pii/S0927650517300166>.
- H. Landt, P. Padovani, E. S. Perlman, and P. Giommi. A physical classification scheme for blazars. *Monthly Notices of the Royal Astronomical Society*, 351(1):83–100, Jun 2004. ISSN 1365-2966. doi: 10.1111/j.1365-2966.2004.07750.x. URL <http://dx.doi.org/10.1111/j.1365-2966.2004.07750.x>.
- M. F. L'Annunziata. Nuclear radiation, its interaction with matter and radioisotope decay. In M. F. L'Annunziata, editor, *Handbook of Radioactivity Analysis (Second Edition)*, pages 1–121. Academic Press, San Diego, 2003. ISBN 978-0-12-436603-9. doi: <https://doi.org/10.1016/B978-012436603-9/50006-5>. URL <https://www.sciencedirect.com/science/article/pii/B9780124366039500065>.
- M. S. Longair. *High Energy Astrophysics*. Cambridge University Press, 2011.
- G. Maier. Introduction into the standard analysis. In *Analysis Workshop, Tucson*, 2014.
- G. Maier and J. Holder. Eventdisplay: An analysis and reconstruction package for ground-based gamma-ray astronomy. In *35th International Cosmic Ray Conference*, 2017.
- K. Mannheim and P. L. Biermann. Gamma-ray flaring of 3C 279: a proton-initiated cascade in the jet. *Astronomy and Astrophysics*, 253:L21–L24, Jan. 1992.
- J. Myers. Fermi gamma-ray space telescope: Exploring the extreme universe, 2016. URL <https://fermi.gsfc.nasa.gov/science/eteu/agn/>.

- A. Mücke and R. Protheroe. A proton synchrotron blazar model for flaring in markarian 501. *Astroparticle Physics*, 15(1):121–136, Mar 2001. ISSN 0927-6505. doi: 10.1016/S0927-6505(00)00141-9. URL [http://dx.doi.org/10.1016/S0927-6505\(00\)00141-9](http://dx.doi.org/10.1016/S0927-6505(00)00141-9).
- N. Park. Performance of the VERITAS experiment. In *34th International Cosmic Ray Conference*, page 771, 2016. doi: 10.22323/1.236.0771.
- A. Petrashyk. *Advancements in Very-High-Energy Gamma-Ray Astronomy with Applications to the Study of Cosmic Rays*. PhD thesis, 2019.
- I. Robson. *Active Galactic Nuclei*. John Wiley, 1996.
- J. D. Scargle. Studies in Astronomical Time Series Analysis. V. Bayesian Blocks, a New Method to Analyze Structure in Photon Counting Data. *The Astrophysical Journal*, 504(1):405–418, Sept. 1998. doi: 10.1086/306064.
- J. D. Scargle, J. P. Norris, B. Jackson, and J. Chiang. Studies in astronomical time series analysis. vi. bayesian block representations. *"The Astrophysical Journal"*, 764(2):167, Feb 2013. ISSN 1538-4357. doi: 10.1088/0004-637x/764/2/167. URL <http://dx.doi.org/10.1088/0004-637X/764/2/167>.
- M. Sikora and G. Madejski. On pair content and variability of subparsec jets in quasars. *The Astrophysical Journal*, 534(1):109–113, may 2000. doi: 10.1086/308756. URL <https://doi.org/10.1086/308756>.
- J. Stanger. *The Bremsstrahlung Synchrotron and Compton effects as emission processes in Astrophysics*, 2004. <http://www.jeffstanger.net/Astronomy/emissionprocesses.html>.
- W. Stecker, F. *Cosmic Gamma Rays*. National Aeronautics and Space Administration, 1971.
- M. C. Stroh and A. D. Falcone. Swift x-ray telescope monitoring of fermi -lat gamma-ray sources of interest. *The Astrophysical Journal Supplement Series*, 207(2):28, Jul 2013.

ISSN 1538-4365. doi: 10.1088/0067-0049/207/2/28. URL <http://dx.doi.org/10.1088/0067-0049/207/2/28>.

- T. Tsen-Yuan Lin. *Measurement of the Bethe-Heitler Cross Section in the TeV Regime and Search for Lorentz Invariance Violation with VERITAS*. PhD thesis, McGill University, 2020.
- R. M. Wagner. *Measurement of very high energy gamma-ray emission from four blazars using the MAGIC telescope and a comparative blazar study*. PhD thesis, Max-Planck institute for physics, 2006.
- S. P. Wakely and D. Horan. TeVCat: An online catalog for Very High Energy Gamma-Ray Astronomy. In *International Cosmic Ray Conference*, volume 3 of *International Cosmic Ray Conference*, pages 1341–1344, Jan. 2008.
- T. C. Weekes, M. F. Cawley, D. J. Fegan, K. G. Gibbs, A. M. Hillas, P. W. Kowk, R. C. Lamb, D. A. Lewis, D. Macomb, N. A. Porter, P. T. Reynolds, and G. Vacanti. Observation of TeV Gamma Rays from the Crab Nebula Using the Atmospheric Cerenkov Imaging Technique. *The Astrophysical Journal*, 342:379, July 1989. doi: 10.1086/167599.
- H. Wilkens, M. Pohl, and J. Kuijpers. Experimental study of high energy muons from extensive air showers in the energy range 100 tev to 10 pev. 01 2003.
- R. Winston. Light collection within the framework of geometrical optics. *J. Opt. Soc. Am.*, 60(2):245–247, Feb 1970. doi: 10.1364/JOSA.60.000245. URL <http://www.osapublishing.org/abstract.cfm?URI=josa-60-2-245>.
- Y. Xue and W. Cui. X-ray flares from markarian 501. *The Astrophysical Journal*, 622(1): 160–167, Mar 2005. ISSN 1538-4357. doi: 10.1086/427933. URL <http://dx.doi.org/10.1086/427933>.